Research Article | Vol. 29, No. 6 / 15 March 2021 / Optics Express 8553
Optics EXPRESS

An extended lidar-based cirrus cloud retrieval scheme: first application over an Arctic site

KONSTANTINA NAKOUDI,[1,2,*] IWONA S. STACHLEWSKA,[3] AND CHRISTOPH RITTER[1]

[1]Alfred Wegener Institute, Helmholtz Centre for Polar and Marine Research, Telegrafenberg A45 Potsdam, 14473, Germany
[2]Institute of Physics and Astronomy, University of Potsdam, Karl-Liebknecht 24/25, 14476, Potsdam, Germany
[3]Faculty of Physics, University of Warsaw (FUW), Warsaw 00-927, Poland
[*]konstantina.nakoudi@awi.de

Abstract: Accurate and precise characterization of cirrus cloud geometrical and optical properties is essential for better constraining their radiative footprint. A lidar-based retrieval scheme is proposed here, with its performance assessed on fine spatio-temporal observations over the Arctic site of Ny-Ålesund, Svalbard. Two contributions related to cirrus geometrical (*dynamic Wavelet Covariance Transform (WCT)*) and optical properties (*constrained Klett*) are reported. The *dynamic WCT* rendered cirrus detection more robust, especially for thin cirrus layers that frequently remained undetected by the classical WCT method. Regarding optical characterization, we developed an iterative scheme for determining the cirrus lidar ratio (LR_{ci}) that is a crucial parameter for aerosol - cloud discrimination. Building upon the Klett-Fernald method, the LR_{ci} was constrained by an additional *reference value*. In established methods, such as the double-ended Klett, an aerosol-free *reference value* is applied. In the proposed *constrained Klett*, however, the *reference value* was approximated from cloud-free or low cloud optical depth (COD up to 0.2) profiles and proved to agree with independent Raman estimates. For optically thin cirrus, the *constrained Klett* inherent uncertainties reached 50% (60-74%) in terms of COD (LR_{ci}). However, for opaque cirrus COD (LR_{ci}) uncertainties were lower than 10% (15%). The detection method discrepancies (dynamic versus static WCT) had a higher impact on the optical properties of low COD layers (up to 90%) compared to optically thicker ones (less than 10%). The *constrained Klett* presented high agreement with two established retrievals. For an exemplary cirrus cloud, the *constrained Klett* estimated the COD^{355} (LR_{ci}^{355}) at 0.28 ± 0.17 (29 ± 4 sr), the double-ended Klett at 0.27 ± 0.15 (32 ± 4 sr) and the Raman retrievals at 0.22 ± 0.12 (26 ± 11 sr). Our approach to determine the necessary *reference value* can also be applied in established methods and increase their accuracy. In contrast, the classical aerosol-free assumption led to 44 sr LR_{ci} overestimation in optically thin layers and 2-8 sr in thicker ones. The multiple scattering effect was corrected using Eloranta (1998) and accounted for 50-60% extinction underestimation near the cloud base and 20-30% within the cirrus layers.

1. Introduction

Cirrus clouds play a key role in the Earth radiative budget. Cirrus are the only cloud genus inducing either cooling or heating at the top of the atmosphere during daytime, with the rest of the clouds producing a cooling effect [1,2]. The relative magnitude of short-wave cooling and infrared warming is highly dependent on the cloud geometrical, optical and microphysical properties [3–5]. Cirrus clouds occur on an average frequency of 40% over the mid-latitudes [6], which maximizes over the tropics (up to 70%) [7] and decreases towards the poles. Arctic ice clouds display highly variable occurrence frequencies, from 25% over Ny-Ålesund, Svalbard, (single layer clouds) [8] up to 50% over Eureka, Nunavut, Canada [9]. However, there is a lack

#414770 https://doi.org/10.1364/OE.414770
Journal © 2021 Received 16 Nov 2020; revised 25 Dec 2020; accepted 11 Jan 2021; published 4 Mar 2021

Optics EXPRESS

of studies focusing on the coverage, geometrical and optical properties of solely Arctic cirrus clouds.

Accurate and precise cirrus cloud detection is of high necessity. Apart from affecting the Earth radiative budget [10], the geometrical cloud thickness is indispensable for parameterization schemes of cirrus cloud optical depth (COD) [11]. Cirrus optical properties have been globally assessed by collocated Cloud-Aerosol lidar with Orthogonal Polarization (CALIOP) and Cloud Profiling Radar measurements, yielding a quite stable cirrus lidar ratio (LR_{ci}, ratio of extinction (α) to backscatter coefficient(β) within the cirrus cloud range) of 33 ± 5 sr over the ocean [12]. However, satellite observations over the poles were limited, with dedicated aircraft campaigns bringing added value through alternated lidar and in-situ cirrus cloud measurements [13]. Cirrus geometrical and optical properties have also been derived from the synergy of active and passive remote sensing [14–17]. Nevertheless, exploiting infrared radiances to detect ice clouds [18,19] and retrieve their optical properties [20,21] is challenging over cold and bright surfaces such as snow and ice.

Lidar systems are capable of delivering vertically resolved geometrical and optical properties of optically thin clouds on fine spatio-temporal scales. Their operating wavelengths, i.e. at ultraviolet, visible and near infrared, are ideal for cirrus studies, as they are more sensitive to small crystal sizes compared to millimeter radar systems [22]. Lidar-relevant cirrus optical properties are the COD, the particulate linear depolarization ratio (LPDR, indicates the sphericity of ice crystals), the LR (indicates type of ice crystals) and the color ratio (CR, ratio of backscatter coefficients at two different wavelengths, indicates the size of ice crystals).

The accuracy of cloud optical properties is critical for high quality radiative effect estimates [23], cloud phase classification [24,25] and cloud – aerosol discrimination (CAD) [17,26–28]. Lofted dust and smoke layers transported into the Arctic, were miss-interpreted as ice clouds in previous CALIOP data releases and motivated their subsequent improvement [29–31]. Conversely, optically thin ice clouds are still frequently miss-classified as aerosols in the polar regions, although the latest CALIOP CAD algorithm has been significantly improved [31–33]. CALIOP cloud phase and CAD algorithms rely on LPDR and CR as a function of temperature, latitude and altitude [31,34]. Thus, ground-based lidar observations that provide similar optical parameters can provide a valuable validation for satellite lidar processing algorithms (e.g. currently CALIOP aboard CALIPSO [35] and imminently ATLID aboard EARTHCARE [36]).

Different lidar-based retrievals of cirrus cloud optical properties exist in literature, such as the transmittance [37–39], the double-ended Klett [40], the backward – total optical depth [41] and the Raman technique [40]. Each of these retrievals has its own strengths and limitations. For instance, the transmittance and backward – total optical depth methods cannot be applied to optically thin cirrus (COD < 0.05 and COD < 0.1, respectively). The Raman technique provides a vertically-dependent LR_{ci} but is limited to night-time applications, contrary to the double-ended Klett method that, however, yields a layer-mean LR_{ci}.

In this study, we propose an extended cirrus cloud retrieval scheme, consisting of detection (*dynamic WCT*) and optical characterization (*constrained Klett*). The scheme is applied on representative cirrus clouds over Ny-Ålesund, Svalbard, and its limitations and strengths are investigated. Sensitivities related to cirrus detection are performed (section 3) and their effect on cirrus optical properties is also examined (section 4.3). The inherent uncertainties of the proposed *constrained Klett* are also quantified (section 4.2). Finally, the *constrained Klett* is compared with two established optical retrievals, namely the double-ended Klett and Raman (section 5), and their limitations and strengths are discussed (section 6). The optical properties are corrected for the multiple scattering effect (Appendix). Cirrus layers are divided in three regimes according to their COD, following the classification of Sassen and Cho (1992) [42] i.e. sub-visible (COD < 0.03), optically-thin (0.03 < COD < 0.3) and opaque cirrus layers (0.3 < COD < 3). Hereafter, the term cirrus cloud will refer to a set of consecutive cirrus layers.

Optics EXPRESS

2. Methods

2.1. Instrumentation and selection of cirrus clouds

In this work, we exploit a unique measurement dataset from the multi-wavelength Koldewey Aerosol Raman lidar (KARL) system, which is installed on the Alfred Wegener Institute – Institute Paul Emile Victor (AWIPEV) research base, Ny-Ålesund (78.9^{o}N, 11.9^{o}E), Svalbard Archipelago. KARL is a powerful so called $3\beta + 2\alpha + 2\delta$ + 2wv system equipped with an Nd:YAG laser that emits pulses of 200 mJ at 1064, 532 and 355 nm with a 50 Hz repetition rate [43]. The receiver comprises a 70 cm diameter telescope with a 2.28 mrad field of view (FOV), while the laser beam divergence amounts to 0.8 mrad. The range of full overlap is 600 m. The combination of photon counting (PC) and analog (A) acquisition mode allows for large dynamical detection range. The specifications of KARL enable high quality signal acquisition at fine vertical and temporal scales (7.5 m, 1.5 min), which are ideal for the investigation of cirrus cloud properties. KARL has been deployed for the evaluation of aerosol optical, microphysical and radiative properties using classical approaches [44–46] or in combination with airborne lidar [47]. However, cloud optical retrievals with KARL were so far underexplored [48].

This study focuses on cirrus clouds and, thus, the presence of supercooled liquid–water layers should be excluded. Therefore, we only considered clouds with temperature lower than -40^{o}C, which is the homogeneous nucleation temperature, at the height of cloud base (C_{base}) and cloud top (C_{top}) [15,26]. Temperature profiles were obtained from radiosondes, which are daily launched at 11 UT from the AWIPEV research base [49–51]. The utilized temperature criterion is quite strong as Shupe (2011) [52] reported only 3-5% liquid water occurrence between -40 and -30^{o}C within Arctic clouds. Thus, the possibility of liquid water presence is very low, even within the range of temperature uncertainty, i.e. sensor related uncertainties or errors due to radiosonde drift and temporal discrepancy with lidar observations.

In the following section we present in detail all the steps of cirrus detection, including the revised method and its newly introduced parameters. In parallel, the main steps are depicted in Fig. 1 and Fig. 2. Note that the code for the revised cirrus detection is publicly available [53].

2.2. Cirrus detection and underlying cloud screening

The Wavelet Covariance Transform (WCT) method [54] was extended with dynamic thresholds for detecting the cirrus C_{base} and C_{top}. The classical WCT method is sensitive to lidar signal vertical gradients and has been employed for detecting either cirrus clouds [55,56] or the planetary boundary layer top height [57–59]. Firstly, the lidar signals were corrected for the dead-time, electronic noise and background illumination effects [43]. Then, the PC and A signal components were glued together as described in Hoffmann (2011) [43]. The gluing interval (several hundred meters zone) was selected as such that both signals were of high quality i.e. non-saturated PC and A with high SNR. Finally, the lidar range-corrected (Pr^2) signal was normalized (with respect to the median signal between the range of full overlap and 12 km). The latter step was essential for making the WCT profiles comparable to those from literature [60] and did not affect the Pr^2 signal and WCT gradients. In Fig. 1 the Pr^2 signal and WCT profiles corresponding to the lower part of a cirrus layer are presented. The WCT profile (Eq. (1)) can be perceived as the low-pass filtered version of the Pr^2 signal [59] as it is based on the convolution of the Pr^2 signal with a Haar step function (Eq. (2)) of specific step width (dilation, α) and step location (b).

$$W_f(\alpha, b) = \frac{1}{\alpha} \int_{C_{base}}^{C_{top}} P(r) \cdot r^2 \cdot h\left(\frac{r-b}{\alpha}\right) dr \tag{1}$$

$$h\left(\frac{r-b}{\alpha}\right) = \begin{cases} +1, & b - \frac{\alpha}{2} \le r \le b \\ -1, & b \le r \le b + \frac{\alpha}{2} \\ 0, & \text{elsewhere} \end{cases} \tag{2}$$

Optics EXPRESS

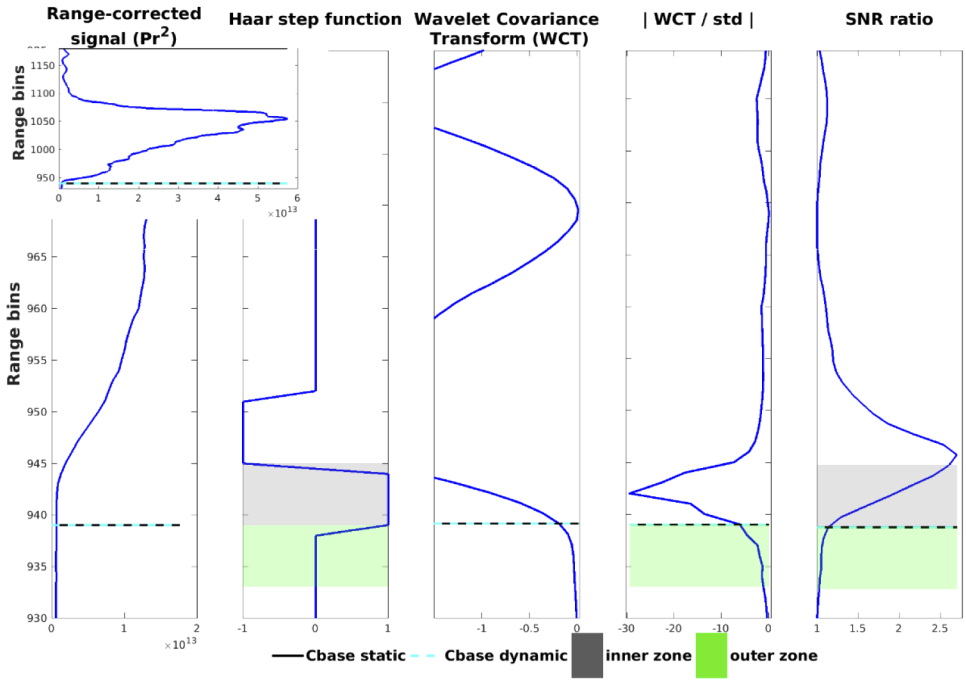

Fig. 1. Exemplary profiles of Pr^2 signal, Haar step function, WCT, WCT to signal standard deviation (std) ratio ($\left|WCT/std\right|$) and *SNR ratio*, which correspond to the lower part of a cirrus layer observed at 7-9 km by KARL over Ny-Ålesund. Horizontal lines denote the dynamic (cyan) and static (black) derived C_{base}. Grey (green) shaded areas denote the half dilation (a/2) zone within (outside) the cirrus layer. The whole cirrus layer Pr^2 profile is given in the upper left inset figure. The signal std was calculated within the outer zone of each range bin.

The Pr^2 signal was integrated within half dilation ($\alpha/2$) below (outer zone, Fig. 1) and above (inner zone, Fig. 1) each range bin. An appropriate dilation is crucial for accurate cirrus detection. A relatively narrow dilation produces more noisy WCT profiles, while a too wide dilation may not resolve small-scale features such as thin clouds. In order to select an appropriate dilation, we assessed its effect on cirrus detection through a sensitivity analysis (section 3.1).

The knowledge of cloud presence below the targeted cirrus layers is important. For this reason, underlying cloud layers were screened with the WCT method. If both the C_{base} and C_{top} were identified below 5 km (6 km), the cloud was flagged as *low-level* (*mid-level*). It should be noted that the low-level Arctic ice clouds and ice fogs are not considered cirrus clouds [22]. Lidar profiles were retained for further evaluation on condition that signal quality was high. Otherwise, if the signal-to-noise ratio (SNR) was decreased (< 3 as in [41]) above the low- or mid-level clouds, the profiles were discarded. Likewise, the signal quality was checked above the cirrus C_{top}. The cirrus detection scheme is outlined in Fig. 2.

2.2.1. Revised detection method: dynamic wavelet covariance transform

A crucial parameter for cirrus detection is the WCT threshold, which determines whether a signal gradient denotes a cirrus layer boundary or not. Static WCT thresholds have been proposed so far [60,61]. However, in this study we introduce dynamic thresholds, which assess the strength of the detected gradients with respect to the given signal variability. The dynamic thresholds

Optics EXPRESS

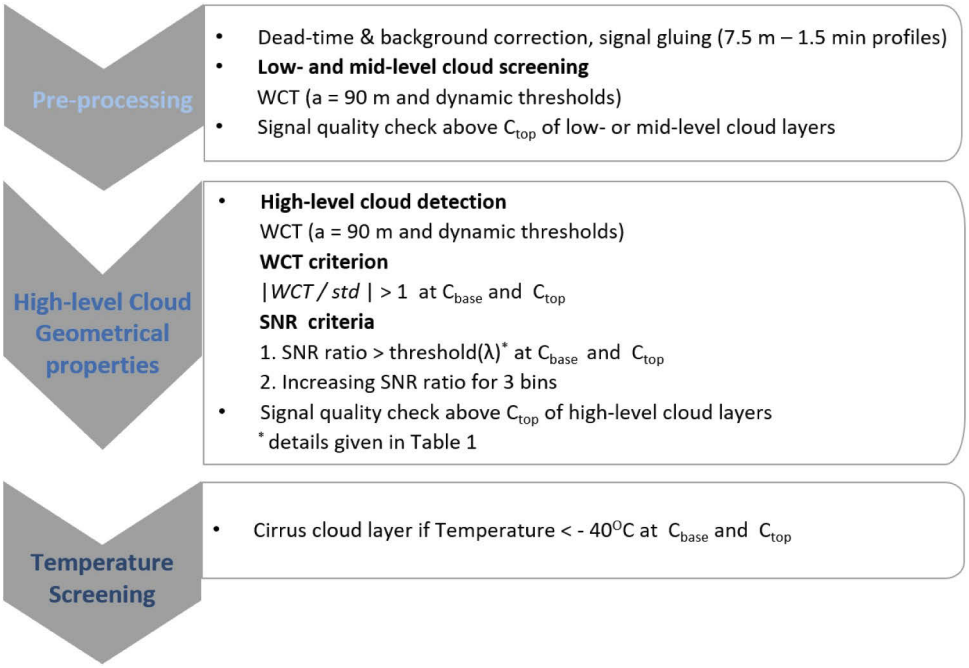

Fig. 2. Flowchart of newly proposed cirrus detection scheme. For details see section 2.2. The cirrus detection algorithm is given in Code 1 [53].

depend on the ratio of WCT over the signal standard deviation ($\left|WCT/std\right|$) as well as on the SNR. This dynamic approach has a higher robustness potential, since it is adaptable to the given cloud strength and lidar specifications. After examining a significant number of characteristic profiles, we found that cirrus peaks were related to WCT values exceeding the signal standard deviation ($\left|WCT/std\right|>1$, e.g. Fig. 1). $\left|WCT/std\right|$ thresholds of 1.5 and 2 were also investigated, but they frequently detected only stronger cirrus parts, leaving out the faint marginal parts. In the upward (downward) direction, a candidate C_{base} (C_{top}) was identified at one bin below (above) the range where $\left|WCT/std\right|>1$.

In order to discriminate cirrus related peaks from noise, an SNR related criterion was also introduced. At each range bin, the median SNR was calculated at $\alpha/2$ bins below and $\alpha/2$ bins above, where α is the dilation of the WCT profile (Fig. 1). More specifically, the median SNR was calculated within the inner and outer zones of bins, where $\left|WCT/std\right|>1$. Then, the algorithm checked whether the inner to outer zone *SNR ratio* exceeded a given threshold in order to make sure that the detected peaks were not related to noise but to a real feature. The above mentioned procedure was performed in the upward (downward) direction for C_{base} (C_{top}) detection. Additionally, an increasing *SNR ratio* was demanded for three consecutive bins above the C_{base} (below the C_{top}). The *SNR ratio* values were found to slightly differ for each wavelength due to differences in the SNR of each channel and are summarized in the Appendix. A more detailed investigation on the WCT wavelength dependency is presented in section 3.2. An assessment of the dynamic thresholds in comparison to the static ones is presented in section 3.3.

In the following section we describe in detail all the steps of the proposed *constrained Klett* method (section 2.3.2), including the newly introduced parameters, i.e. the *convergence range*,

Optics EXPRESS

the estimated reference backscatter ratio (BSR_{ref}) as well as the recursive LR_{ci} process and the factor used to adjust the LR_{ci} after each iteration (Eq. (3)). Moreover, we depict the steps in Fig. 4 to outline the methodology. Note that we have made publicly available the code of the *constrained Klett* [53].

2.3. Cirrus optical characterization

2.3.1. Temporal averaging within stationary periods

High vertical (7.5 m) and temporal (1.5 min) resolution profiles allowed for reliable cirrus detection. However, the precision of optical properties was affected by statistical uncertainties (signal noise and *reference value* uncertainty) and, thus, temporal averaging was desirable. Nonetheless, care should be taken with long temporal averaging to avoid smearing out the cloud physical variability i.e. to avoid averaging cloud and cloud-free range bins and produce physically unrealistic profiles. More importantly, distorted particulate extinction (α_{part}) profiles affect the accuracy of radiative effect estimates [23].

Bearing the aforementioned aspects in mind, we adopted a temporal averaging that is constrained by periods of stationarity following Lanzante (1996) [62]. This procedure is based on the Mann–Wilcoxon–Whitney test, such that the data points of one stationary period share the same COD statistical distribution [62]. This method has already been applied to time-series of cirrus COD and geometrical thickness by Larroza et al. (2013) [39]. In this study, the procedure was applied on the integrated backscatter coefficient (β_{int}) time-series , which was obtained from an initial guess Klett-Fernald retrieval. The designation of stationary (yellow lines) and temporal (red lines) averaging periods is shown for the case of 23 January 2019 in Fig. 3. The β_{int} was selected instead of the COD because the latter might be influenced by the assumed LR_{ci}. However, for the majority of the cirrus clouds analyzed over Ny-Ålesund (2011-2020) the β_{int} and COD exhibited similar variability.

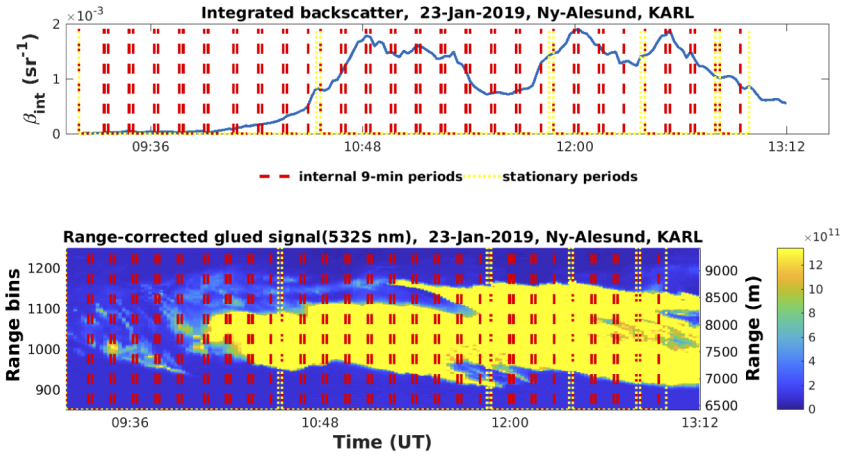

Fig. 3. Time-series of integrated backscatter (β_{int}, upper panel) and height-time plot of Pr^2 signal (lower panel) with overlaid stationary (yellow lines) and 9-min periods (red lines). Lidar observations were obtained on 23 January 2019 with KARL over Ny-Ålesund, Svalbard. Temporal averaging was only performed within each stationary period.

As expected the stationary periods have variable duration, since they reflect the physical variability of the investigated parameter. For instance, on 23 January 2019, each of the first two periods (9:11-10:19 and 10:20-11:54 UT) was over one-hour long, while the subsequent two periods (11:55-12:26 and 12:28-12:47 UT) did not exceed 30 min each. However, one should keep in mind that the β_{int} is a columnar quantity and, thus, the cirrus vertical variability cannot

Optics EXPRESS

be accounted for by the stationary periods. Therefore, shorter averaging periods were obtained for ensuring non distorted profiles. In order to obtain homogeneous statistical uncertainties we constructed temporally averaged profiles of equal duration (9 min by averaging 6 consecutive raw profiles) within each stationary period. Gaps (no measurement or no cirrus detection) and periods shorter than 9 min were discarded. The cirrus C_{base} and C_{top} were newly determined by applying the *dynamic WCT* method on the averaged Pr^2 profiles.

2.3.2. Proposed optical retrieval: constrained Klett method

An extended method for cirrus optical retrievals is proposed, hereafter mentioned as *constrained Klett*. A backward Klett–Fernald retrieval [63,64] was employed, constrained by the backscatter ratio (BSR), which is the ratio of molecular and particulate backscatter over molecular backscatter, beneath the cirrus cloud. The LR_{ci} was iteratively adjusted until the BSR matched with a reference BSR value (BSR_{ref}). The main steps of the *constrained Klett* method are outlined in Fig. 4. The *constrained Klett* algorithm is given in Code 1 [53]. The *constrained Klett* made use of the assumption that the aerosol content beneath the cirrus cloud was invariable. In order to enhance the validity of this assumption, the near-range *reference value* (also called calibration value) was set within the range of minimum Pr^2 signal variance (*convergence range*). The *convergence range* was bounded between the full overlap range (600 m) and 1 km beneath the minimum C_{base}. In this way, artificial signal gradients as well as cirrus adjacent areas, where turbulence and ice seeding are more likely, were avoided. The *convergence range* was a 500 m-zone, where the median Pr^2 signal presented minimum temporal variance. When the variance was equally low in more than one zones, the higher zone was selected, because the Klett errors increase with the integration from the far range. In order to further enhance the validity of aerosol content stability assumption, profiles not highly correlated with the temporal median profile ($r < 0.98$) were discarded.

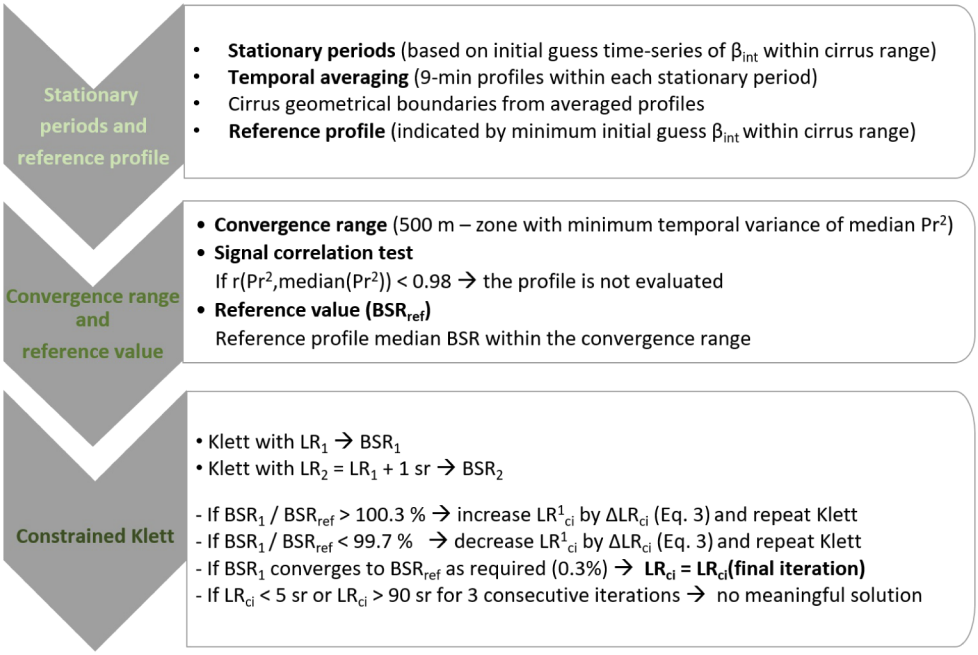

Fig. 4. Flowchart of configuration procedure (section 2.3.1) and optical characterization (section 2.3.2) with *constrained Klett* method. The *constrained Klett* algorithm is given in Code 1 [53].

Optics EXPRESS

An initial guess Klett–Fernald retrieval was first performed using two LR zones, one within the cirrus layer (assumed LR_{ci}^{355} = 20 sr and LR_{ci}^{532} = 28 sr) and one zone outside (assumed LR^{355} = 35 sr and LR^{532} = 36 sr). The LR_{ci} values were needed for initializing the Newton-Raphson method and they can be arbitrary provided that they are close enough to the unknown quantity [65]. Therefore, the LR_{ci} initial values were selected close to those most frequently reported by other studies (e.g. [56,66–68]). Regarding the LR values outside the cirrus layer we used background values for the site of Ny-Ålesund based on statistics provided by Ritter et al. (2016) [69]. These LR values should be adapted accordingly for different lidar sites.

Subsequently, the β_{int} within the cirrus range was estimated. Although the β_{int} was an initial guess, its minimum corresponded to low COD layers. The lower the β_{int} the lower the effect of a wrongly chosen LR_{ci} on the Klett solution. Therefore, the *reference profile* corresponded to the profile of minimum β_{int} or to a temporally close cloud-free profile (if available). The BSR_{ref} was estimated from the *reference profile* as the median BSR within the *convergence range*. In section 4.1 we investigate the upper COD limit for deriving an accurate BSR_{ref}. The effect of BSR_{ref} statistical uncertainties on the optical properties is also investigated (section 4.2).

Once the *convergence range*, the *reference profile* and the BSR_{ref} were defined, the recursive Klett procedure was initiated. Two initial guess Klett retrievals were performed, one with LR_{ci}^{1} and another with $LR_{ci}^{2} = LR_{ci}^{1} + 1$ sr (see lower part of Fig. 4). Upon each iteration, the median BSR within the *convergence range* was estimated (BSR_1 and BSR_2 as derived from the retrieval with LR_{ci}^{1} and LR_{ci}^{2}, respectively). When the ratio of BSR1 over BSRref exceeded the desirable *convergence percentage* (set to 0.3% after sensitivity analysis, see section 4.2), the LR_{ci} was adjusted by a factor ΔLR_{ci} (Eq. (3)). Following the Newton–Raphson method (described in Ryaben'kii and Tsynkov (2006) [65]), the ΔLR_{ci} factor was formulated as the difference of BSR_{ref} and BSR_1 over the difference of BSR_1 and BSR_2, the latter being equivalent to $\frac{\partial BSR}{\partial LR}$ with dLR = 1 sr.

$$\Delta LR_{ci} = \frac{BSR_{ref} - BSR_1}{BSR_1 - BSR_2} \tag{3}$$

The iterative process was bounded by physically meaningful LR_{ci} values, i.e. between 5 sr and 90 sr. A wide range of bounding LR_{ci} values was employed as we did not want to a priori exclude physically possible LR_{ci} values. The selection was based on previous experimental (at different locations) [40,70] and modeling studies [71–73]. For instance, Ansmann et al. (1992) [40] reported values between 5-15 sr over a marine mid-latitude site, using the Raman technique. Chen et al. (2002) [70] reported over Taiwan LR_{ci} values lower than 10 sr in some cases. Okamoto et al. (2019) and (2020) [72,73] performed modeling simulations and reported LR_{ci} values at 355 and 532 nm starting from approximately 5 sr and exceeding 100 sr for 2-D plates depending on the effective angle between the particle symmetrical axis and the laser beam (Fig. 5 from Okamoto et al. (2019) [72], Fig. 8 and Fig. 9 from Okamoto et al. (2020) [73]).

The retrieval was considered successful once the BSR_1 solution matched with the BSR_{ref}. The resulting β_{part} and vertically-constant LR_{ci} were used for estimating the COD according to Eq. (4):

$$\mathrm{COD} = \int_{C_{base}}^{C_{top}} LR_{ci} \cdot \beta_{part}(r) dr \tag{4}$$

2.3.3. Existing optical retrievals: double-ended Klett and Raman

In order to gain confidence in the proposed *constrained Klett* method, two established retrievals were also applied, namely the double-ended Klett and Raman [40]. Concerning the constrained Klett, different sets of backward and forward Klett–Fernald retrievals [63,64] were performed with changing LR_{ci} value. The LR_{ci} resulting in the lowest *root mean square error* between the backward and forward β_{part} profiles was selected. The LR_{ci} was modified within physically expected values of 5 and 90 sr as in the *constrained Klett* [40,70–73]. In this work the

Optics EXPRESS

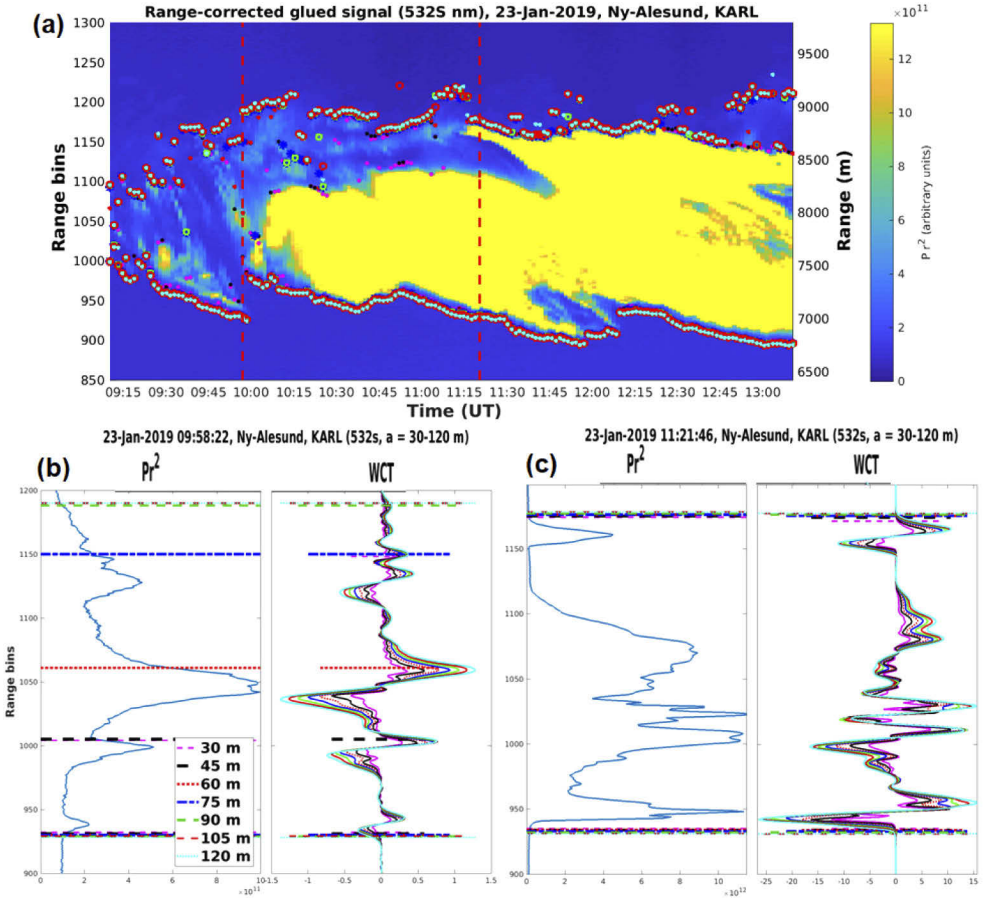

Fig. 5. Height-time plot of lidar Pr^2 signal (a). Different symbols present the C_{base} and C_{top} resulting from dilation values between 30 and 120 m. Red vertical lines (panel a) denote the selected profiles of Pr^2 and WCT (presented in panels b and c). Higher inter-dilation spread was observed for smooth-shaped boundaries (b).

Klett–Fernald calibration window was set in the stratosphere for the backward retrieval and in the *convergence range* for the forward retrieval. In this way, the retrieval was comparable to the *constrained Klett*. However, it should be noted that the classical double-ended Klett method assumes zero β_{part} below and above the cirrus cloud [40]. The impact of this aerosol-free assumption is investigated in section 5.

The cirrus optical characterization and the BSR_{ref} estimation was also performed via the Raman technique. This technique provides the backscatter and extinction coefficients independently [40] and, thereby, a vertically-dependent LR_{ci} can be derived. In this study, we report the vertically averaged Raman derived LR_{ci} to facilitate the comparison with *constrained Klett* (section 2.3). The α_{part} at 355 and 532 nm is based on the rotational-vibrational Raman signals of 387 and 607 nm, respectively. Since the Raman cross-sections are orders of magnitude smaller than the elastic scattering cross-sections, the Raman technique is usually limited to night-time applications. In order to reduce the noise of the weak Raman signals, profiles were smoothed with a Savitzky–Golay filter [74]. The smoothing window was equal to one-third of the minimum cirrus cloud thickness. The molecular number density, which is needed for estimating the α_{part}, was derived by collocated radiosonde ascents from the AWIPEV research base. The Ångström

Optics EXPRESS

exponent of ice crystals for the wavelength pairs of 355-387 nm and 532-607 nm was assumed equal to unity. This is a reasonable assumption since the size of the ice crystals is usually sufficiently large compared to the ultraviolet and visible wavelengths [40]. Raman extinction uncertainties stem from statistical signal noise and uncertainties in molecular number density, which were, however, low within the cirrus layers. The comparison between the *constrained Klett*, the double-ended Klett and Raman retrievals is presented in section 5 and their limitations and strengths are discussed in section 6.

2.4. Multiple scattering correction

The effect of multiple scattering cannot be neglected when the size of the scatters is large compared to the emitted wavelength. The effect is more pronounced if the lidar system has a wide telescope FOV and a non-negligible laser beam divergence. The multiple scattering effect does not only depend on the COD but also on ice crystal effective radius (r_{eff}) and laser beam cloud penetration depth. For this reason, an analytical model is needed in order to correct for high order scattering events. In this study, we used the multiple scattering correction (MSC) model of Eloranta (1998) [75], which is openly available (http://lidar.ssec.wisc.edu/multiple_scatter/ms.htm). The Eloranta model assumes the presence of hexagonal ice crystals for phase function calculations. Moreover, a mono-disperse ice crystal vertical distribution was assumed. The ice crystal r_{eff} was estimated as a quadratic function of temperature, following the parameterization of Wang and Sassen (2002) [76] given by Eq. (5):

$$r_{eff} = 90.14 + 0.659 \cdot T - 0.004 \cdot T^2 \tag{5}$$

The model simulates the ratio of up to seven-order (P_{tot}) to single scattering photon power (P_1) as a function of range (r) and wavelength (λ). Sensitivity tests revealed that higher than three-order scattering events contributed negligibly to the total photon power. Therefore, the first four scattering orders were finally taken into account as a compromise between accuracy and computational speed. Initially, the apparent α_{part}, denoted as α_{app} (or β_{part} multiplied by the LR_{ci}) was incorporated into the MSC model. Subsequently, a first estimation of the multiple scattering factor F(λ,r) (Eq. (6)) and the quasi-corrected extinction ($\alpha(\lambda, r)$) (Eq. (7)) were obtained:

$$F(\lambda, r) = \frac{\frac{d}{dr} \ln \frac{P_{tot}(r)}{P_1(r)}}{2 \cdot \alpha_{app}(\lambda, r) + \frac{d}{dr} \ln \frac{P_{tot}(r)}{P_1(r)}} \tag{6}$$

$$\alpha(\lambda, r) = \frac{\alpha_{app}(\lambda, r)}{1 - F(\lambda, r)} \tag{7}$$

As a next step, the quasi-corrected $\alpha(\lambda, r)$ was incorporated again into the MSC model. This recursive procedure was repeated until the MSC model converged to a stable F(λ,r). Usually, only two iterations already provided sufficient convergence. A similar procedure was followed in previous studies [56,66,68]. A simplified MSC approach, which is only dependent on the COD was introduced by Platt (1973) [14] and is frequently used in literature ([42,70]). Eq. 8 describes the simple MSC factor n, with the MSC COD being the ratio of the apparent COD over the factor n. The analytical and simplified MSC approaches are compared in the Appendix.

$$n = \frac{COD}{e^{COD} - 1} \tag{8}$$

3. Sensitivities on cirrus geometrical properties

3.1. Wavelet covariance transform - dilation sensitivity

Since the WCT dilation is an important parameter for accurate and precise cirrus detection (section 2.2), a relevant sensitivity analysis is performed here. Thanks to the high vertical

Optics EXPRESS

resolution (7.5 m) of KARL signals, we explored small dilation values between 30 m (4 range bins) and 120 m (16 range bins), presented with different symbols in Fig. 5. After analyzing a significant number of cirrus layers, it was observed that dilation values smaller than 90 m were less sensitive to smooth-shaped cirrus layers, as shown in Fig. 5(b) (smooth signal gradients close to C_{top}). On the contrary, the 90 m dilation was more effective for faint layers and efficiently captured layers thinner than 200 m layers, as for 7:30-9:00 UT on 23 January 2019 (Fig. 5(a)). Detecting faint layers near the C_{base} is important, since the multiple scattering effect is higher there ([77] and Appendix of this study). Overall, the discrepancies arising from the dilation selection were low, with the majority of inter-dilation spread being lower than 50 m.

3.2. Wavelet covariance transform - wavelength dependency

The dependency of cirrus detection on wavelength was assessed both by the dynamic and static WCT methods. Since the SNR depends on background illumination conditions, both daytime (25 April 2015, Fig. 6(a)) and night-time (23 January 2019, Fig. 6(b)) cirrus clouds were investigated. In Fig. 6(a) and 6(b) the dynamic (open symbols) and static (dot symbols) WCT derived boundaries are demonstrated for different wavelengths. Thin and faint cirrus layers were not so discernible in the 355 nm channel with parallel polarization (355_p - cyan symbols) as in the other wavelengths due to the strong UV Rayleigh scattering (Fig. 6(b), for example at 8:30–10:00 UT). This behavior was more profound for the static WCT method. Concerning the 355 nm channel with perpendicular polarization (355_s - black symbols), this was strongly affected by noise during daytime (Fig. 6(a)), with noise peaks frequently detected even with increased *SNR ratio* thresholds. In the 532_p channel (green symbols) both the static and dynamic methods mostly detected the stronger cirrus parts (Fig. 6(a), for example at 14:00–16:00 UT).

The cirrus layer presented in Fig. 6(c) was characterized by smooth-shaped C_{base} and strong-shaped C_{top}. Therefore, the discrepancies across different wavelengths were larger for the C_{base}. The static (dotted lines) and dynamic (dashed lines) WCT derived boundaries are given for the different channels. The 355_p and 532_p channels detected mostly central cirrus parts. In contrast, the 355_s, 532_s (light green) and 1064 nm (red symbols) channels were more sensitive to faint marginal parts and showed better inter-agreement, especially for the dynamic method. Moreover, the SNR of the perpendicular polarization channels was higher compared to those with parallel polarization and the SNR_{532} was higher than SNR_{355}. In general, longer wavelengths perform better in discriminating clouds from aerosol. However, the KARL system records 1064 nm signals in analog mode, which is more prone to noise.

For the aforementioned reasons, the 532_s channel was finally selected for cirrus detection as the longest wavelength and highest quality available channel. It should be mentioned, however, that under specific conditions the 532_s derived boundaries also presented variability. For instance, fluctuating geometrical boundaries can be seen at 8:00–10:00 UT (Fig. 6(b)) due to weak gradients, especially close to the C_{top}. Variability was also revealed during 13:00–14:00 UT (Fig. 6(b)), with weak signal gradients overhead of strong ones. This variability was lower for temporally averaged signals thanks to higher SNR. The optimal *SNR ratio* thresholds for each channel of KARL are given in the Appendix.

3.3. Dynamic - static wavelet covariance transform comparison

In the following, the *dynamic WCT* method is compared to the static one. Both methods were applied on 532_s signals using a 90 m dilation. Two daytime cirrus layers (Fig. 7(b) and 7(c)), which were highly affected by background illumination, are analyzed in detail. The dynamic method was more sensitive to weak signal gradients that, however, exceeded the signal standard deviation. For instance, on 25 April 2015, 7:59 UT (Fig. 7(b)), the cirrus layer presented -0.07

Optics EXPRESS

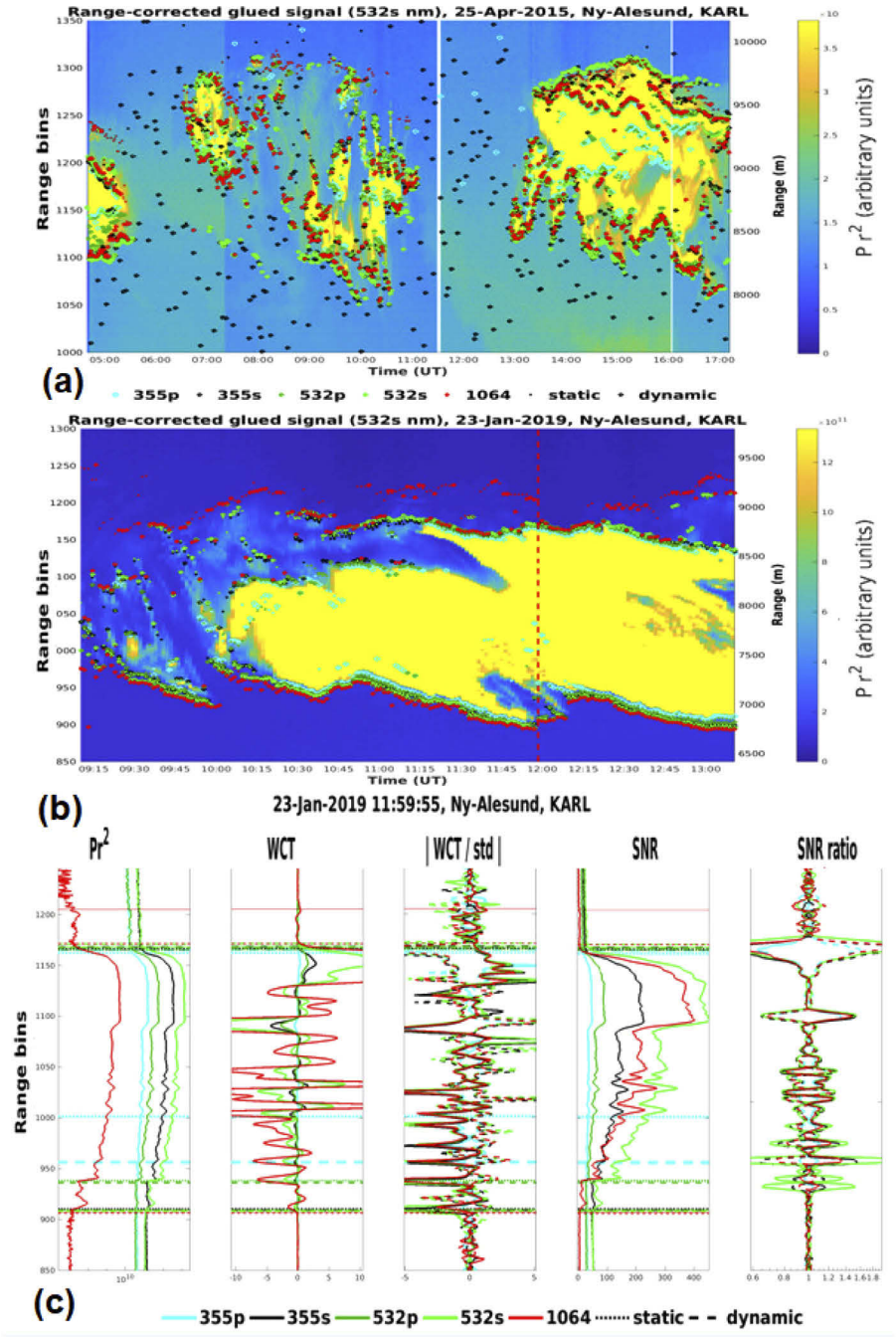

Fig. 6. Height-time plot of lidar Pr^2 signal for daytime (a) and night-time (b) cirrus clouds. Overlaid with different colors are the cirrus geometrical boundaries as derived by the dynamic (open markers) and static (dot markers) WCT method. Selected profiles of Pr^2, WCT, $\left|WCT/std\right|$, SNR and *SNR ratio* are presented together with the dynamic (dashed lines) and static (dotted lines) WCT derived boundaries (c). The 532_s channel was finally selected for cirrus detection.

Optics EXPRESS

WCT and $\left|WCT/std\right|$ equal to 3 at the C_{base}. Therefore, the C_{base} of this cirrus layer was not detectable with the static method (0.3 WCT threshold, see [61]).

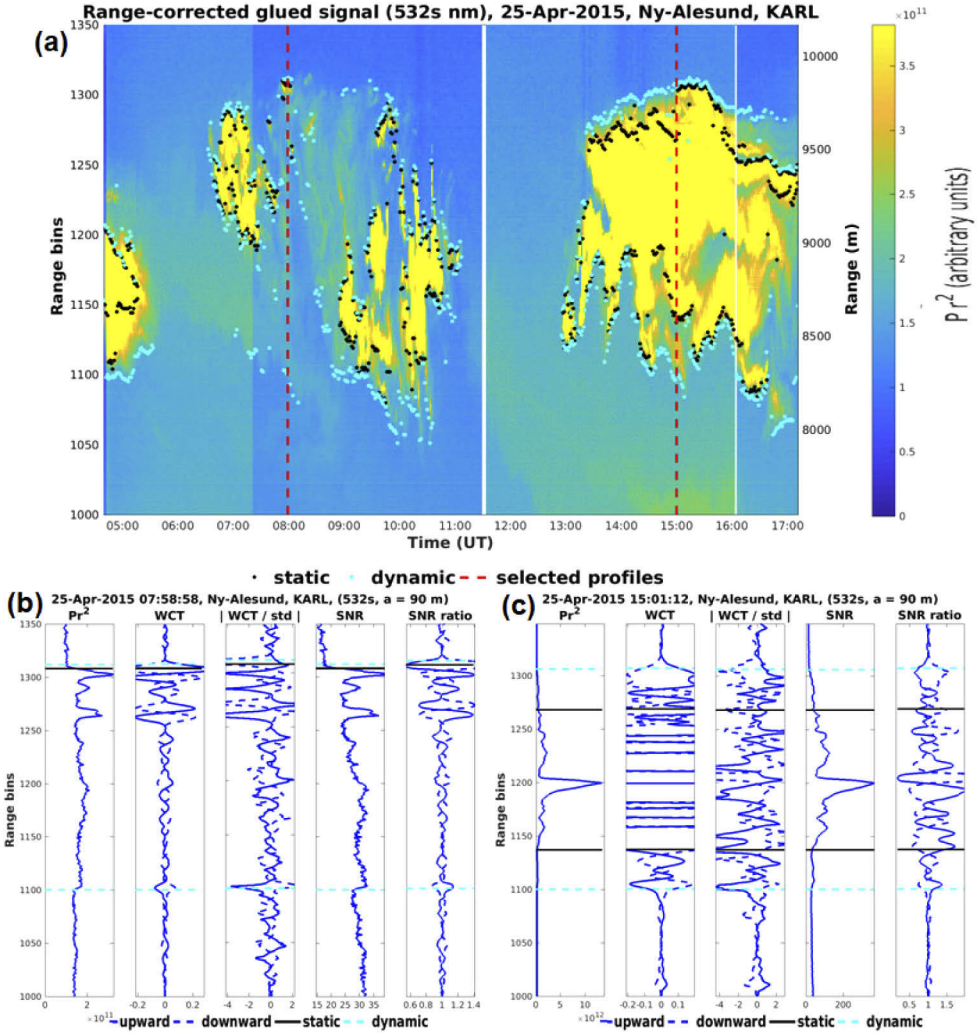

Fig. 7. Height-time plot of lidar Pr^2 signal with overlaid dynamic (cyan) and static (black) WCT derived cirrus boundaries. Signal normalization accounts for background color changes (see section 2.2). Selected profiles are denoted with red vertical lines (a) and presented in panels (b) and (c), where horizontal lines indicate the dynamic and static cirrus boundaries. Solid (dashed) blue lines correspond to upward (downward) profiles used for C_{base} (C_{top}) detection. The *dynamic WCT* was more sensitive to faint and marginal parts of cirrus layers.

Another strength of the dynamic method lies on its increased sensitivity to marginal cirrus layers. On 25 April 2015, 15:01 UT (Fig. 7(b)), the static method was only sensitive to stronger cirrus parts, while the dynamic method detected the C_{base} (C_{top}) 277.5 m (285 m) out of the static-derived boundaries. Hence, the cirrus geometrical thickness was underestimated by more than 500 m by the static method. Increased sensitivity to cirrus marginal layers is also an important advancement of the latest CALIOP CAD algorithm. More details will be discussed in section 6. It should be mentioned that sometimes both the dynamic and static WCT methods

Optics EXPRESS

failed to detect the cirrus boundaries, especially for faint cirrus layers, as for 8:00–9:00 UT on 25 April 2015 (Fig. 7(a)). Overall, the dynamic method detected faint cirrus layers that otherwise could not have been detected by the static method.

4. Accuracy and uncertainty assessment

4.1. Reference value accuracy and limitations

The cirrus cloud of 23 January 2019 was selected for assessing the accuracy and inherent uncertainties of *constrained Klett*, since it comprised different regimes from sub-visible to lower opaque layers [42]. Concerning the *reference value* (see section 2.3.2), this was calculated from a cloud-free profile ($BSR_{ref}^{cloud-free}$) observed at 7:47-7:56 UT prior to the cirrus cloud passing over Ny-Ålesund. The *convergence range* (see section 2.3.2) was selected at 5.5– 6 km, where the signal temporal variance was minimum. The BSR_{ref} accuracy was evaluated by estimating the same quantity via the Raman technique (BSR_{ref}^{Raman}). This analysis is illustrated in Fig. 8. The blue line and shaded area (median ± standard deviation) denote the $BSR_{ref}^{cloud-free}$, while the BSR_{ref}^{Raman} (black symbols) and BSR_{ref}^{guess} (blue symbols) are also presented.

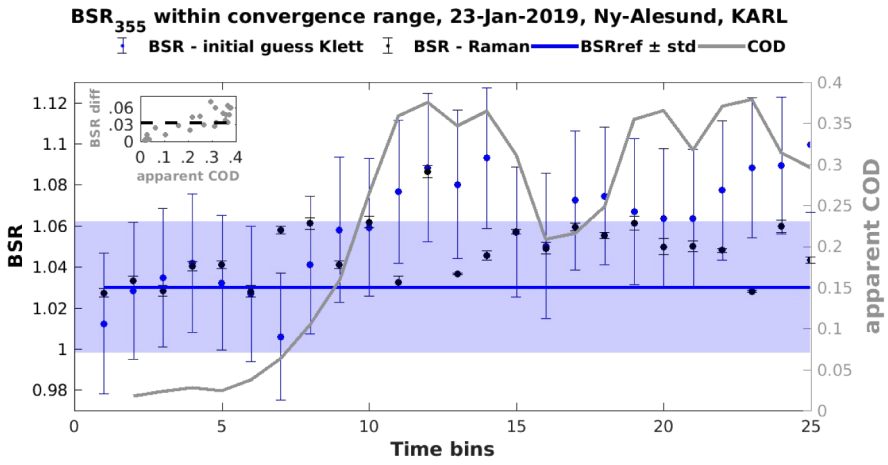

Fig. 8. BSR^{355} within the *convergence range* (median ± standard deviation) as derived by the initial guess Klett (BSR_{ref}^{guess}, blue symbols) and Raman retrievals (BSR_{ref}^{Raman}, black symbols). BSR_{ref}^{Raman} errorbars are smaller due to a 75 m-smoothing of the BSR profile. For comparison, a preceding cloud-free profile provided the $BSR_{ref}^{cloud-free}$ (blue line and shaded area denote its median ± standard deviation). The apparent COD is given on the right axis. The difference between BSR_{ref}^{guess} and $BSR_{ref}^{cloud-free}$ versus the apparent COD are presented in the upper left inset figure. A sufficiently accurate BSR_{ref}^{guess} can be obtained from cirrus layers with 0.2 maximum COD. The BSR_{ref}^{guess} mostly agrees with BSR_{ref}^{Raman} within the range of uncertainties.

At 355 nm (532 nm, not shown) the initial guess Klett provided a median ± standard deviation $BSR_{ref}^{cloud-free}$ of 1.03 ± 0.03 (1.07 ± 0.02), while the Raman yielded BSR_{ref}^{Raman} equal to 1.06 ± 0.01 (1.06 ± 0.02). $BSR_{ref}^{cloud-free}$ and BSR_{ref}^{Raman} were in agreement within the range of uncertainties, this being satisfactory, taking into account the high Raman statistical uncertainties especially for fine temporal scales (here 9 min). Thus, the BSR_{ref} parameter was estimated with sufficient accuracy.

Optics EXPRESS

If cloud-free profiles were not available, the minimum β_{int} (or COD) profile would have been selected as *reference profile* (see section 2.3.2). However, in such cases the BSR_{ref} accuracy would have been subject to an upper COD limitation. More specifically, the lower the cirrus COD the more accurate is the BSR_{ref}^{guess} expected to be, with the impact of a wrongly assumed LR_{ci} on the initial guess Klett being lower. In order to quantitatively assess the effect of COD on the BSR_{ref}^{guess} accuracy, we compared the BSR_{ref}^{guess} with BSR_{ref}^{Raman} for every single profile of the 23 January 2019 cirrus. Then, we assessed up to which COD the BSR_{ref}^{guess} accuracy is acceptable. As it can be seen, a sufficiently accurate BSR_{ref}^{guess} can be obtained for COD up to 0.2 (Fig. 8, right axis). This is illustrated more clearly on the upper left inset figure, with the BSR_{ref}^{guess} lying within the $BSR_{ref}^{cloud-free}$ uncertainty (dashed line) for 0.2 maximum COD. Hence, even if the minimum COD profile (here time bin 1) was selected instead of a cloud-free profile, the resulting BSR_{ref}^{guess} would have agreed with the $BSR_{ref}^{cloud-free}$ and BSR_{ref}^{Raman}.

Another significant remark concerns the aerosol content stability beneath the cirrus cloud, which is assumed both by the constrained and double-ended Klett retrievals. As displayed in Fig. 8, the BSR_{ref}^{Raman} variability lied within the uncertainty of the $BSR_{ref}^{cloud-free}$ *reference value*, indicating that the stability assumption was valid. Finally, it should be underlined that the upper COD limitation discussed above only concerns the *reference profile* selection. As long as a sufficiently accurate BSR_{ref} is obtained, the *constrained Klett* can be applied on any cirrus cloud regime.

4.2. Inherent uncertainties of constrained Klett

In order to assess the inherent uncertainties, we investigated the response of cirrus optical properties to the parameters of the *constrained Klett* method, namely the *convergence percentage* and *reference value* BSR_{ref} (see section 2.3.2). In the first sensitivity analysis (Fig. 9(a)) the *convergence percentage* was modified between 0.1% and 0.5%, with 0.3% being the default. The LR_{ci} of optically thinner layers was more sensitive (maximum spread 10% or 3 sr) compared to thicker layers (maximum spread 5%). Overall, the COD was modified by less than 0.004 (1-10% spread depending on the COD). Less strict *convergence percentage*s (higher than 1%, not shown) were incapable of constraining the LR_{ci} with acceptable accuracy.

The impact of BSR_{ref} statistical uncertainties on the optical properties was also evaluated (Fig. 9(b)). In the control case, the median value (BSR_{ref} = 1.03) was used, while in the perturbed cases the BSR_{ref} was increased by 0.01 (blue symbols), 0.02 (grey symbols) and 0.03 (cyan symbols). These uncertainties were typically encountered during the analysis of different cirrus clouds (2011-2020) over Ny-Ålesund, Svalbard. Low COD layers (corresponding to time bins 1–5) were more sensitive to the BSR_{ref} parameter. More specifically, if the BSR_{ref} was perturbed too far from the control case, reasonable results were not always possible to obtain. Therefore, an accurate BSR_{ref}^{guess} is crucial. The LR_{ci} displayed higher sensitivity for optically thinner layers (14–19 sr or 74 and 60% with respect to control values of 19 sr and 32 sr). Lower sensitivity (less than 3 sr or 13% with respect to control value of 24 sr) was found for opaque layers. The COD sensitivity was higher for lower optically-thin and opaque regimes, varying between 0.02 and 0.03 (7-50% with respect to control values of 0.3 and 0.06) for the most perturbed case.

4.3. Effect of geometrical boundaries on the optical properties

In the following we assess the effect of cirrus detection method on the apparent optical properties. To this end, the cirrus geometrical properties were determined via the dynamic (Fig. 10(a), cyan symbols) and static WCT methods (black symbols). Based on the dynamic and static derived boundaries, we retrieved the optical properties via the *constrained Klett* and investigated the resulting discrepancies (Fig. 10(b)). The optical discrepancies are illustrated as a function of

Optics EXPRESS

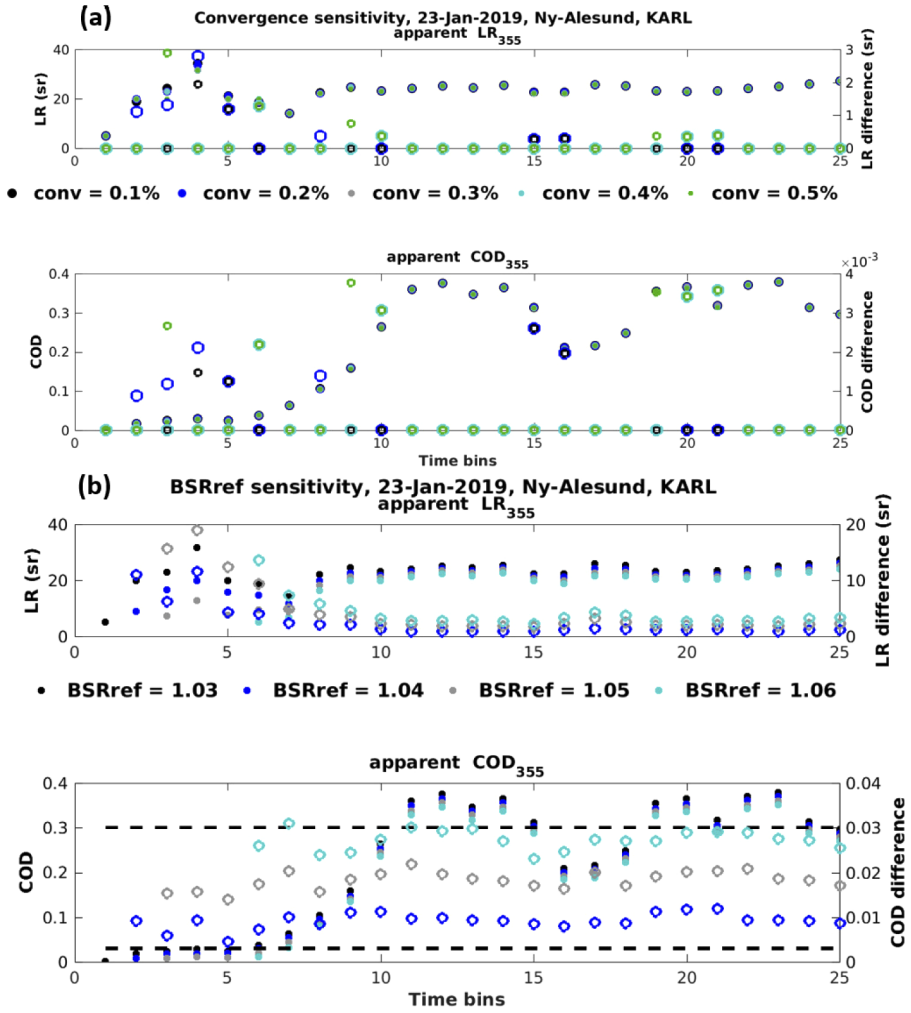

Fig. 9. Sensitivity of optical properties with respect to the *convergence percentage* (a) and the *reference value* (BSR_{ref}, b) parameters of the *constrained Klett*. Absolute differences with respect to the control case are presented with open symbols on the right axis. Dashed horizontal lines denote the optically-thin and sub-visible COD regimes according to [42]. Optically thinner layers displayed higher sensitivity, especially with respect to the BSR_{ref} parameter.

Optics EXPRESS

geometrical discrepancies (symbol size). As geometrical discrepancies we defined the cumulative difference of C_{base} and C_{top} between the static and dynamic method.

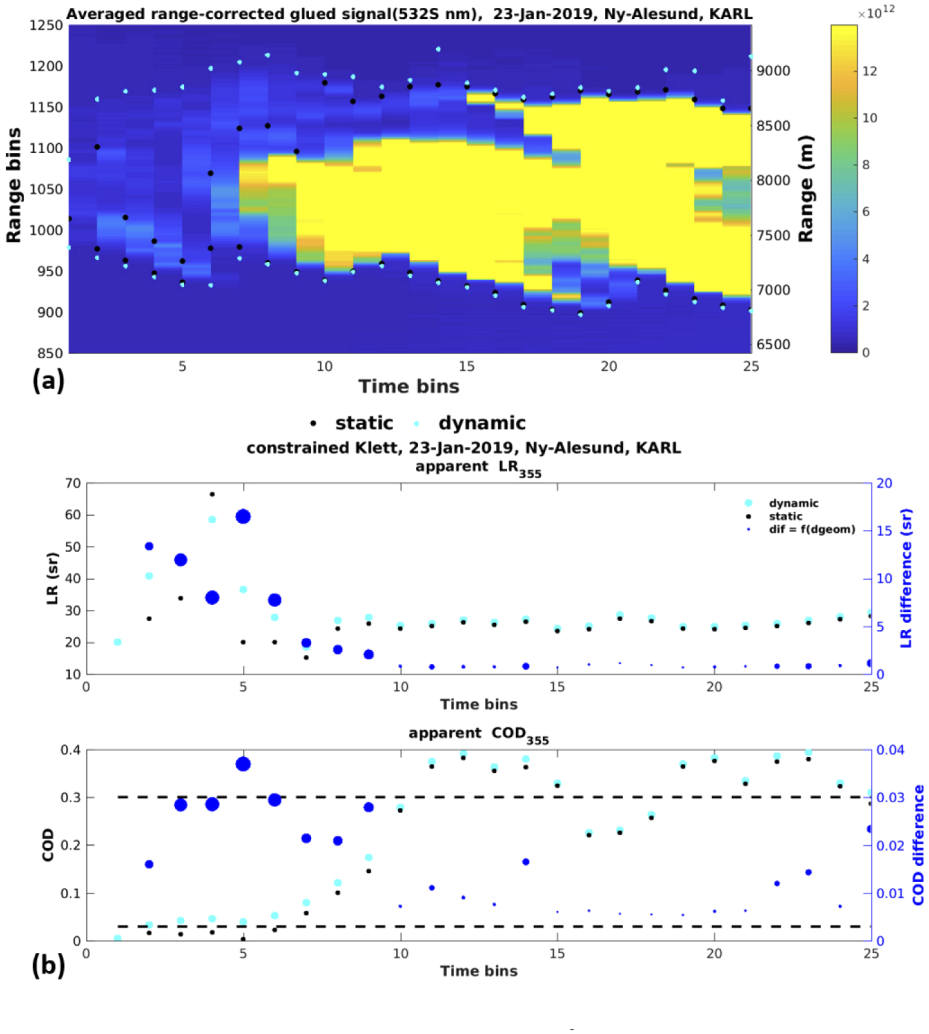

Fig. 10. Height-time plot of temporally averaged Pr^2 signal with overlaid dynamic (cyan) and static (black) WCT cirrus boundaries (a). Corresponding optical properties as derived by the *constrained Klett* method (b) and differences (blue dots) as a function of the geometrical discrepancy (dot size). The geometrical discrepancies varied from 30 to 1613 m. Optically thinner layers were affected more intensely.

Higher geometrical discrepancies mostly occurred for faint cirrus layers (Fig. 10(a)). The dynamic method provided higher COD values, since thanks to its higher sensitivity, it usually yielded wider boundaries. Higher optical discrepancies arose for upper sub-visible and optically thin layers. The highest LR_{ci} and COD differences (45% or 17 sr and 93% or 0.037, respectively) were related to the maximum geometrical discrepancy (1613 m). The geometrical discrepancy, however, was a necessary but not sufficient condition for optical discrepancies to occur. More specifically, in opaque layers despite the non-negligible geometrical discrepancy (up to 490 m), the LR_{ci} and COD solution discrepancies were low (less than 1 sr and 0.025, respectively). This indicates that the solution converges faster within the main part of optically thicker layers

Optics EXPRESS

thanks to sufficient light attenuation and, thus, marginal parts play a less critical role. Overall, for optically thin and opaque layers the LR_{ci} difference was lower than 10% (3 sr) and the COD difference did not exceed 8% (0.025). Finally, one should bear in mind that the MSC optical discrepancies are expected to be higher than the apparent ones, which were presented here. The same sensitivity is performed on the double-ended Klett and Raman derived optical properties in the Appendix.

5. Inter-comparison of cirrus optical properties

The comparison of *constrained Klett* derived optical properties with those from the double-ended Klett and Raman retrievals is shown for the cirrus cloud of 23 January 2019. The *dynamic WCT* method provided the C_{base} at 7 ± 0.2 km and C_{top} at 8.8 ± 0.2 km, with the ambient temperature at -48 and -63^{o}C, respectively. The MSC LR_{ci}^{355} and COD^{355} as derived from the different retrievals are presented in Fig. 11. More details on the multiple scattering effect are given in the Appendix.

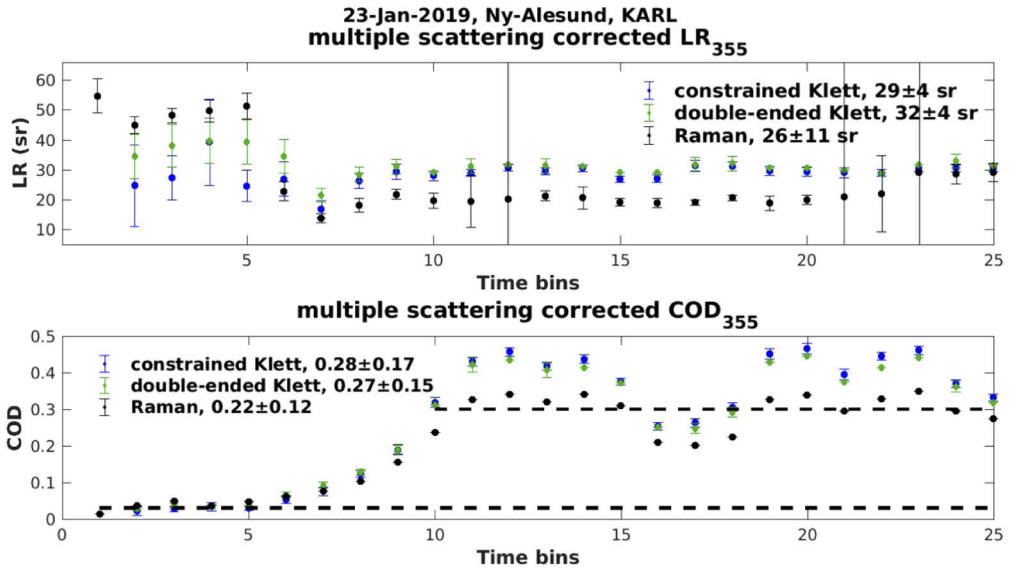

Fig. 11. Inter-comparison of *constrained Klett*, double-ended Klett and Raman retrievals in terms of MSC optical properties at 355 nm (mean ± standard deviation given in the legend). For Klett retrievals, errorbars represent uncertainties due to 0.01 BSR *reference value* error. For the Raman method, LR_{ci} errorbars represent the standard error of the mean (extremely high for vertically inhomogeneous layers), while COD errorbars represent the integral-propagated α_{part} uncertainty.

The double-ended and *constrained Klett* exhibited high agreement, especially in the COD. The Raman technique provided lower vertically-averaged LR_{ci} and COD solutions, probably because of the vertical smoothing process. Higher LR_{ci} discrepancies occurred for layers with COD lower than 0.1. This could be attributed to less efficient convergence of the *constrained Klett* as well as to higher Raman statistical uncertainties. The mean (± standard deviation) discrepancy between constrained and double-ended Klett amounted to 3 ± 4 sr for LR_{ci}^{355} (1 ± 2 sr for LR_{ci}^{532}) and 0.01 ± 0.007 for COD^{355} (0.02 ± 0.02 for COD^{532}). The corresponding discrepancies between *constrained Klett* and Raman were equal to 10 ± 6 sr for LR_{ci}^{355} (14 ± 12 sr for LR_{ci}^{532}) and 0.07 ± 0.04 for COD^{355} (0.06 ± 0.06 for COD^{532}). Overall, the three retrievals exhibited agreement within the range of uncertainties on the mean cloud optical properties. The COD^{355} (LR_{ci}^{355}) was estimated 0.28 ± 0.17 (29 ± 4 sr) by the *constrained Klett*, 0.27 ± 0.15 (32 ± 4 sr) by the

Optics EXPRESS

double-ended Klett and 0.22 ± 0.12 (26 ± 11 sr) by the Raman retrievals. Similar agreement was found for the optical properties at 532 nm (not shown). The optical properties are comparable to those derived, via double-ended Klett and Raman retrievals, over the sub-Arctic site of Kuopio (62.7 ^{o}N) with COD^{355} of 0.25 ± 0.2 and LR_{ci}^{355} of 33 ± 7 sr [56].

The high agreement between the double-ended and *constrained Klett* retrievals can be attributed to the fact that both rely on elastic signals. There is an additional reason, however, behind this agreement. In this study, we used identical far- and near-range *reference values* for both methods in order to make them as comparable as possible. Nevertheless, we should underline that the classical double-ended Klett is based on aerosol-free assumptions above and below the cirrus cloud [40]. Therefore, we performed a sensitivity analysis to assess the impact of the latter assumption. In Fig. 12, the LR_{ci} and COD are presented as in Fig. 11 but the double-ended Klett with aerosol-free assumptions (BSR = 1) is additionally given. As revealed, optically thinner layers (time bins 1 to 5) were the most affected ones by the aerosol-free assumption, displaying LR_{ci} of 75 ± 7 sr (mean ± standard deviation). Previously, the LR_{ci} was assessed at 31 ± 2 sr by the double-ended Klett, 24 ± 5 sr by the *constrained Klett* and 38 ± 5 sr by the Raman retrieval. For optically thicker layers the aerosol-free assumption led to positive discrepancies (2–8 sr) as well, while the overall COD discrepancies lay between 0.01 and 0.03. Hence, the LR_{ci} was overestimated since the amount of extinction that was overlooked due to the aerosol-free assumption was instead attributed to the cirrus layers. Consequently, a non-realistic BSR_{ref} assumption can make a fundamental difference in the solution accuracy.

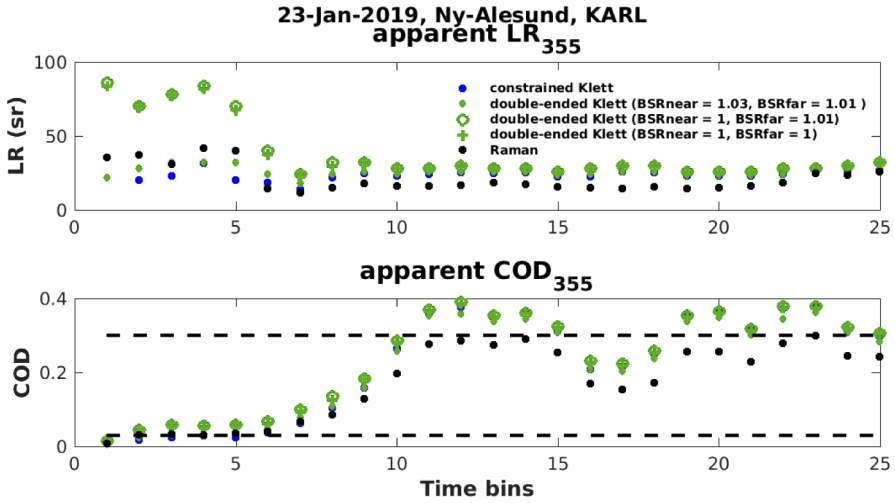

Fig. 12. Same as Fig. 11 except for apparent optical properties and additional double-ended Klett with aerosol-free assumptions (BSR = 1). Non-realistic *reference values* can introduce biases in the optical properties, especially for optically thinner layers (44 sr average LR_{ci} bias).

The *constrained Klett* method was applied to a large number of cirrus layers with variable vertical structure, geometrical and optical thickness observed at different altitudes both during day-time and night-time. The LR_{ci} and COD distributions as obtained from the three different retrievals, i.e. *constrained Klett*, double-ended Klett and Raman (when applicable) presented high similarities both at 355 and 532 nm. Moreover, it was found that LR_{ci} close to the bounding values (5 and 90 sr) were associated with cirrus layers of low geometrical depth and COD. For these regimes cirrus detection and optical characterization is more challenging (section 3.3, 4.2, 4.3 and Appendix) and therefore care will be taken when providing long-term cirrus properties statistics (e.g. exclude cirrus layers with COD lower than 0.02).

Optics EXPRESS

6. Discussion

6.1. Limitations of existing cirrus cloud retrievals

The limitations of cirrus optical retrievals already existing in literature are briefly discussed here. Starting with the transmittance method, it relies on the ratio of backscattering signals at C_{base} and C_{top}, which is quadratively proportional to the cirrus layer transmission [37–39]. However, the transmittance method cannot converge adequately for optically thinner cirrus (COD below 0.05) [70]. Concerning the backward - total optical depth method [41], this derives an initial guess COD via the slope method. Then, an α_{part} profile is obtained by a backward or forward Klett and, finally, it is modified to match with the initial guess COD. Nevertheless, the slope method requires negligible molecular extinction and backscatter contribution within the cloud, clear air at C_{base} and C_{top} and negligible multiple scattering effect. Therefore, no reasonable accuracy can be achieved either for optically thinner cirrus (COD below 0.1) or in the presence of overhead aerosol layers. Finally, the Raman technique [40] is typically limited to night-time applications because it relies on the weak Raman signals (section 2.3.3). Therefore, Raman signals are usually smoothed vertically at the expense of effective resolution [78] and clustered over long temporal periods. However, distorted α_{part} profiles might be produced, with ice crystal related peaks being suppressed, having a critical impact on the accuracy of radiative effect estimates [23]. Exemplarily, vertical smoothing of 780 m can lead to biases of 64% (7.7 Wm^{-2}) at surface and 39% (11.8 Wm^{-2}) at top of the atmosphere for opaque cirrus layers [23]. Likewise long temporal averaging that smears out the cirrus physical variability, is expected to induce radiative effect biases. Therefore, an application of high-resolution daytime profiling, an approach developed for Raman lidar (as in [79]) is in our upcoming research interests.

6.2. Strengths and limitations of extended cirrus cloud retrieval

Cirrus detection and optical characterization is, in general, more challenging for geometrically and optically thinner cirrus layers. However, the proposed *dynamic WCT* method proved to be more sensitive to faint cirrus layers that were partly or completely overlooked by the static method (section 3.3). A similar advancement has been achieved in the 4^{th} version of CALIOP CAD algorithm [31], which shows increased sensitivity to optically thinner layers adjacent to cirrus clouds (cirrus fringes). At the same time, however, miss-classification into aerosol increased slightly, as a side effect of higher calibration accuracy and increased sensitivity to high altitude depolarizing aerosol. Consequently, there is still place for improvement in the CALIOP CAD algorithm. The optical biases, which result from cirrus boundary miss-determination and can be relatively high for optically thinner layers (section 4.3 and Appendix), render CAD optimization crucial. To this end, the satellite-derived cirrus geometrical properties can be evaluated by ground-based lidar observations and, thereby, the CAD thresholds might be improved. Added value can be brought by ground-based lidar observations in the Arctic, where miss-classification issues are frequently reported [31–33].

The *dynamic WCT* method enables the investigation of optically thinner layers (section 3.3) that are, however, characterized by higher inherent uncertainties (section 4.2) and more challenging LR_{ci} value adjustment process(section 2.3.2). From a numerical viewpoint, the *constrained Klett* cannot always provide a robust LR_{ci} value for low COD layers. The light attenuation within such layers is not sufficiently strong to scale the solution and appoint the best match. Likewise the double-ended Klett solutions exhibit lower absolute differences and, hence, the best matching solution is more challenging to find. Based on our analysis, the *constrained Klett* adjusts effectively the LR_{ci} for apparent COD as low as 0.02 for both 355 and 532 nm. Comparable minimum COD values were reported over the sub-Arctic site of Kuopio ($COD^{355} = 0.24 \pm 0.21$ and $COD^{532} = 0.22 \pm 0.2$ [56]). In this respect, the *constrained Klett* is expected to be more

Optics EXPRESS

robust for mid-latitude and tropical cirrus (accompanied by cloud-free profiles to ensure an accurate BSR_{ref}), the majority of which fall into the optically thin regime [55,66–68].

In this study, we demonstrated that highly accurate optical properties can be derived solely by a stable backward Klett retrieval, as long as an additional *reference value* is appointed beneath the cirrus cloud. More importantly, the near-range *reference value* is not simply assumed but approximated by an initial guess BSR value (BSR_{ref}^{guess}). This is a step towards more accurate retrievals, as this initial guess proved to agree with independent Raman estimates (section 4.1), as long as low COD (below 0.2) *reference profile*s are selected. This upper COD limitation was only encountered in a minority of the analyzed cases over Ny-Ålesund (2011-2020). Even for mid-latitude and tropical cirrus, this limitation is nearly raised as the majority of these clouds mostly belong to the optically thin regime [55,66–68]. It should also be pointed out that our system KARL is not in *24/7* operation and, thus, cirrus clouds were neither monitored from their formation nor clear-sky observations prior to the cirrus passing were always available. However, for continuously operating lidar systems as those of the Micro-Pulse Lidar Network (MPLNET) [80] the maximum COD limitation can be lifted more easily.

One can benefit from the highly accurate near-range *reference value* proposed here, even if the double-ended Klett is applied. As demonstrated in section 5, the double-ended Klett aerosol-free assumption can lead to LR_{ci} positive biases (Fig. 12), especially in optically thinner layers. Further limitations of the *constrained Klett* relate to the assumed as vertically-independent LR_{ci}. However, this is a common limitation in existing methods such as the transmittance, double-ended Klett and backward - total optical depth. Finally, the aerosol content stability assumption beneath the cirrus cloud proved valid (Fig. 8) according to independent Raman estimates.

7. Summary and outlook

In this study, we explored the limitations and strengths of an extended cirrus cloud retrieval scheme. The scheme is based on lidar observations and comprises newly proposed cirrus detection (*dynamic WCT*) and optical characterization (*constrained Klett*). Cirrus clouds observed over the Arctic research site of Ny-Ålesund, Svalbard, were used for evaluating its performance. The WCT method (section 2.2) [54], which is sensitive to signal gradients, was revised for C_{base} and C_{top} detection. For the first time, two *dynamic WCT* criteria were introduced (section 2.2.1). The first one was related to the ratio of WCT over the signal standard deviation ($\left|WCT/std\right|$). The second criterion compared the SNR in marginal cirrus areas to the SNR of adjacent areas (*SNR ratio*). Cirrus optical properties were derived by a newly introduced iterative Klett–Fernald method [63,64], called *constrained Klett* (section 2.3.2). The novelty of *constrained Klett* is the recursively determined LR_{ci} that was constrained by an additional *reference value* (BSR_{ref}) beneath the cirrus cloud. The BSR_{ref} was estimated either from cloud-free profiles or profiles with minimum cirrus influence (COD up to 0.2). The main findings of this study can be summarized as follows:

- Increased sensitivity to thin cirrus layers (less than 200 m) was achieved thanks to the *dynamic WCT* method and the high vertical resolution (7.5 m) of KARL signals. The *dynamic WCT* method was more sensitive to faint layers, which were, in some cases, partly or completely missed by the static method (section 3). Fine-scale temporal averaging (9 min) was only performed within periods of physical stationarity to obtain non-distorted profiles (section 2.3.1).

- The *constrained Klett* was applicable to all cirrus regimes for COD values down to 0.02. The *reference value* (BSR_{ref}) was highly accurate, since it agreed with independent Raman estimates. Even without cloud-free reference profiles, accurate BSR_{ref} estimates were obtained from layers with COD up to 0.2 (section 4.1).

Optics EXPRESS

- The main *constrained Klett* inherent uncertainty was related to the *reference value* (BSR_{ref}) parameter. Optically thinner layers displayed higher sensitivity (up to 50% in the COD and 60-74% in the LR) induced by typical BSR_{ref} uncertainties (section 4.2). However, the inherent uncertainties were lower (10% in the COD and 15% in the LR) for opaque layers.
- The detection method (dynamic versus static WCT) affected the optical retrievals more critically in optically thinner layers, with COD underestimation by the static method reaching 90% (section 4.3 and Appendix). This underestimation might lead to miss-classification from the optically-thin into the sub-visible regime. Upper optically thin and lower opaque layer errors were lower than 10% in the double-ended and *constrained Klett* retrievals, whereas the Raman errors reached 30% in the LR and 12% in the COD.
- The *constrained Klett* derived optical properties (section 5) agreed within the range of uncertainties with those from the double-ended Klett and Raman retrievals. For an exemplary cirrus cloud, the COD^{355} (LR_{ci}^{355}) was estimated at 0.28 ± 0.17 (29 ± 4 sr) by the *constrained Klett*, 0.27 ± 0.15 (32 ± 4 sr) by the double-ended Klett and 0.22 ± 0.12 (26 ± 11 sr) by the Raman retrievals. Contrary, when the classical aerosol-free assumption was applied in the double-ended Klett, the agreement was significantly lower.
- As a step towards more accurate optical retrievals, the *constrained Klett* near-range *reference value* was not simply assumed, as in classical approaches (e.g. double-ended Klett), but approximated by an initial guess BSR value (BSR_{ref}). Established approaches can benefit from the more realistic *reference value*. Based on sensitivity analysis with aerosol-free conditions assumed, the double-ended Klett overestimated the LR_{ci} by 44 sr in optically thin layers and by 2-8 sr in thicker ones (section 5).
- The multiple scattering effect, which was corrected using the Eloranta analytical model [75], was significant in all cirrus regimes (Appendix). But for MSC, the extinction would have been underestimated by 50-60% near the C_{base} and 20-30% within the cirrus. A simplified MSC approach [14], depending only on the COD, underestimated the MSC for low COD (less than 0.1) layers, especially in terms of the LR_{ci} (by 30%). Conversely, for an opaque layer the simplified MSC approach overestimated the COD (by 50%) and LR_{ci} (by 85%).

The *dynamic WCT* method proposed here can also be applied for detecting the planetary boundary layer top height, with optimized specific modifications. The *constrained Klett* can be employed towards more accurate aerosol retrievals in scenes with broken clouds aloft. This can be achieved through a more realistic estimate for the LR of broken clouds. As a next step, we are going to investigate the long-term variability of cirrus properties over Ny-Ålesund, Svalbard, based on the *dynamic WCT* and *constrained Klett* schemes, with the dataset to be made publicly available. In the future, it is worth comparing and reviewing different cirrus detection schemes (e.g. static and *dynamic WCT* as well as simple multi-scale algorithms [54,81]) based on synthetic lidar signals, while the potential effect of multiple scattering on cirrus detection needs investigation.

Appendix

Selected dynamic wavelet covariance transform thresholds

The proposed thresholds of $\left|WCT/std\right|$ and *SNR ratio* are presented here and summarized in Table 1. The *SNR ratio* was investigated separately at C_{base} and C_{top} due to changes in the signal noise, with higher ratios prescribed at C_{top}. Due to increased noise, stricter *SNR ratio* values were selected for the 1064 nm and the daytime 355_s profiles (see Fig. 6(c)). Less strict

Optics EXPRESS

thresholds were assigned to the 532_s channel, which was finally selected for cirrus detection (section 3.2). The proposed thresholds worked well for cirrus clouds appearing in different altitudes. A sensitivity test is recommended before applying the *SNR ratio* thresholds to systems with different specifications than KARL, since the SNR is dependent on the operating wavelength, averaging time and background illumination conditions. A sensitivity on the $|WCT/std|$ threshold is not necessary as this parameter displayed high stability for different wavelengths and averaging periods.

Table 1. Proposed dynamic $|WCT/std|$ and *SNR ratio* thresholds for each channel. Static thresholds from Baars et al. (2016) [61] are also given.

	WCT threshold		SNR ratio threshold		SNR
channel (nm)	dynamic	static	dynamic C_{base}	dynamic C_{top}	static
355_p	$\|WCT/std\|>1$	0.1	1.1	1.2	>2
355_s	$\|WCT/std\|>1$	0.1	1.2 (d) / 1.1 (n)	1.5 (d) / 1.2 (n)	>2
532_p	$\|WCT/std\|>1$	0.3	1.1	1.3	>2
532_s	$\|WCT/std\|>1$	0.3	1.1	1.2	>2
1064	$\|WCT/std\|>1$	0.3	1.2	1.5	>2

Effect of geometrical boundaries on the optical properties: double-ended Klett and Raman retrievals

Here we evaluate the impact of detection method (dynamic versus static WCT) on the optical properties derived by the double-ended Klett and Raman retrievals (Fig. 13), following the same rational as in section 4.3, where the effect on the *constrained Klett* was examined. Regarding the double-ended Klett (Fig. 13(a)), the discrepancies were higher for optically thinner cirrus. Maximum LR_{ci} and COD differences amounted to 20% (8 sr) and 90% (0.04) for a low COD layer. For opaque layers the LR_{ci} and COD discrepancies did not exceed 10% (2 sr and 0.025). Concerning the Raman technique (Fig. 13(b)), maximum discrepancies occurred within a low COD layer and amounted to 65% (25 sr) for the LR_{ci} and to 95% (0.034) for the COD, probably due to higher impact of noise on the retrievals. Within optically thicker layers the discrepancies did not exceed 30% (6 sr) in the LR_{ci} and 12% (0.03) in the COD.

Multiple scattering correction for different cirrus cloud regimes

Here we investigate the effect of multiple scattering on the optical properties of sub-visible (Fig. 14(a)), optically-thin (Fig. 14(b)) and opaque layers (Fig. 14(c)) observed over Ny-Ålesund by KARL. Primarily, the Eloranta MSC model [75] was employed with corrections based on Eq. (6) and Eq. (7) and then a comparison to the simplified MSC (Eq. (8)) was made. The investigation was performed separately for the α_{part} derived by the Klett and Raman retrievals. In Fig. 14 the apparent and corrected α_{part}^{355} profiles are presented together with the multiple scattering factor (F). The MSC simulations revealed 50-60% α_{part} underestimation near the C_{base}, as presented by Wandinger (1998) [77], which dropped to 20-30% within the layer and typically got negligible near the C_{top}. In ranges with high α_{part} variability, F was oscillating (Fig. 14). It should be noted that the multiple scattering effect was significant in all cirrus regimes. Overall, for the cirrus cloud of 23 January 2019, the vertically-mean F (equal to mean α_{part}

Optics EXPRESS

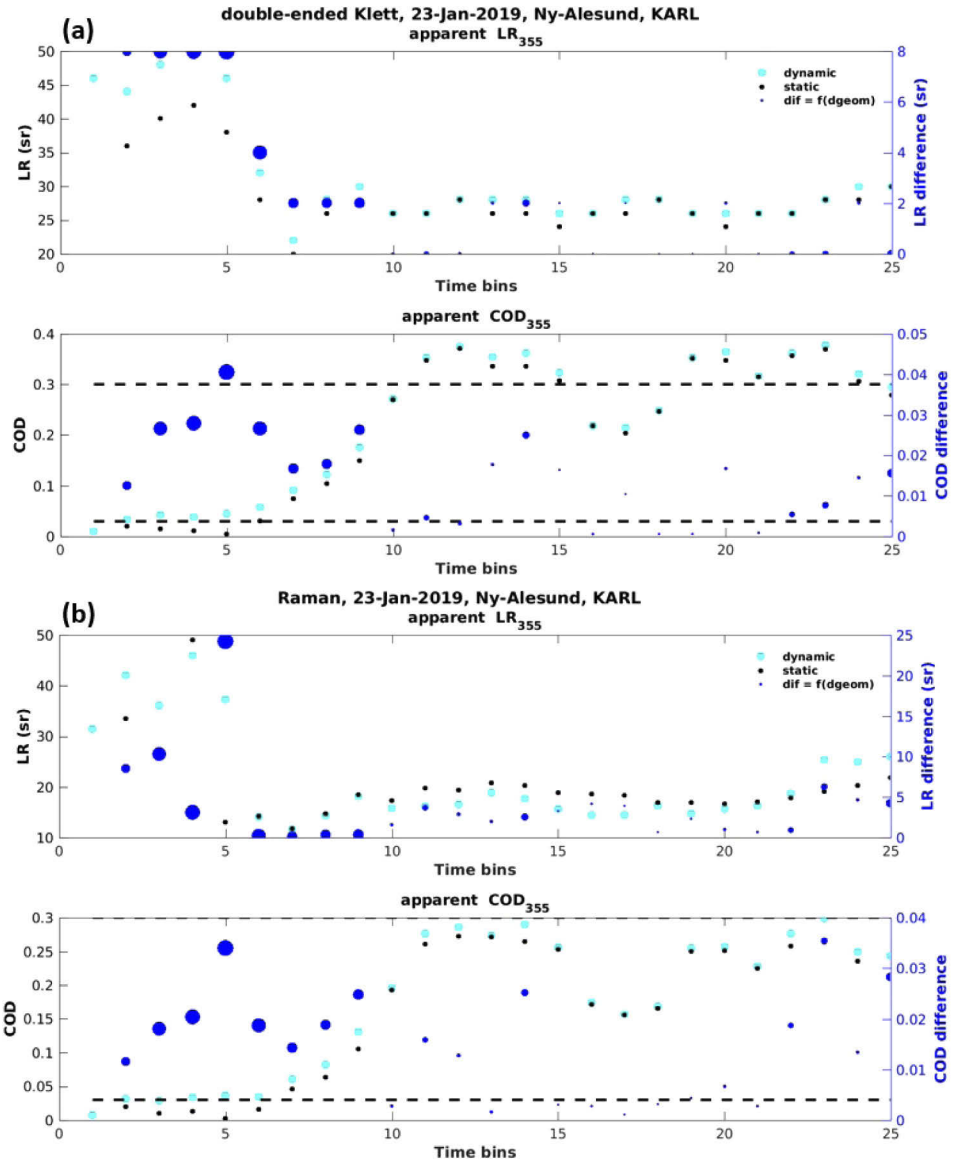

Fig. 13. Same as Fig. 10, except for the double-ended Klett (a) and Raman derived optical properties (b). Higher dynamic - static induced discrepancies were found for optically thinner cirrus layers.

Optics EXPRESS

biases) amounted to 0.11–0.23 for Klett and 0.1–0.43 for Raman. For the upper opaque layer of 24 January 2013 (Fig. 14(c)) F was on average higher.

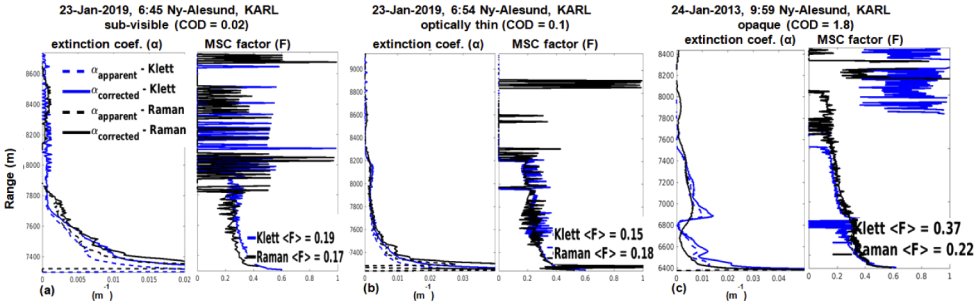

Fig. 14. Profiles of apparent and corrected extinction and MSC factor (F) at 355 nm for sub-visible (a), optically-thin (b) and opaque cirrus layers (c). The MSC was important for all cirrus regimes, amounting to 50-60% near the C_{base} and 20-30% within the cirrus layers. The vertically-mean F is given in the legend.

Our analysis showed that the simplified MSC factor underestimated the MSC within sub-visible and optically-thin layers, especially in terms of the LR_{ci}. The simplified LR_{ci} bias reached 30% (9 sr) for Klett and 38% (15 sr) for Raman retrievals. Conversely, for opaque layers the simplified factor overestimated significantly the Klett COD (by 50% or 1.4) and LR_{ci} (85% or 27 sr) as well as the Raman LR_{ci} (by 40% or 22 sr). Multiple scattering events are more common in the UV compared to visible and infrared wavelengths due to stronger forward scattering [68]. The present investigation, however, that was also applied to α_{part}^{532} (not shown) did not clearly show such a behavior. The MSC at 532 nm was mostly comparable to that of 355 nm.

Funding. Deutsche Forschungsgemeinschaft (268020496–TRR 172).

Acknowledgments. Konstantina Nakoudi wholeheartedly thanks the members of the Remote Sensing Laboratory at the Faculty of Physics, University of Warsaw, for their academic hosting and support. We are thankful to Dr. Edwin Eloranta for developing and making publicly available the multiple scattering correction model. We appreciate the scientific discussions with Dr. Roland Neuber, Dr. Marion Maturilli and Dr. Elina Giannakaki. The long-term support and technical development of KARL at the AWIPEV research base by Wilfried Ruhe and Ingo Beninga, Impres GmbH, are more than appreciated. We are thankful to Dr. Jan Chylik for proof-reading our manuscript. We gratefully acknowledge the funding by the Deutsche Forschungsgemeinschaft (DFG, German Research Foundation) - Project Number 268020496 - TRR 172, within the Transregional Collaborative Research Center - ArctiC Amplification: Climate Relevant Atmospheric and SurfaCe Processes, and Feedback Mechanisms $(AC)^3$. Finally, we would like to thank the three anonymous reviewers that improved this work through their comments.

Disclosures. The authors declare no conflicts of interest.

References

1. S. Lolli, J. R. Campbell, J. R. Lewis, Y. Gu, and E. J. Welton, "Technical note: Fu–Liou–Gu and Corti–Peter model performance evaluation for radiative retrievals from cirrus clouds," Atmos. Chem. Phys. **17**(11), 7025–7034 (2017).
2. J. R. Campbell, D. A. Peterson, J. W. Marquis, G. J. Fochesatto, M. A. Vaughan, S. A. Stewart, J. L. Tackett, S. Lolli, J. R. Lewis, M. I. Oyola, and E. J. Welton, "Unusually deep wintertime cirrus clouds observed over the Alaskan subarctic," Bull. Am. Meteorol. Soc. **99**(1), 27–32 (2018).
3. P. Yang, K.-N. Liou, L. Bi, C. Liu, B. Yi, and B. A. Baum, "On the radiative properties of ice clouds: Light scattering, remote sensing, and radiation parameterization," Adv. Atmos. Sci. **32**(1), 32–63 (2015).
4. E. Kienast-Sjögren, C. Rolf, P. Seifert, U. K. Krieger, B. P. Luo, M. Krämer, and T. Peter, "Climatological and radiative properties of midlatitude cirrus clouds derived by automatic evaluation of lidar measurements," Atmos. Chem. Phys. **16**(12), 7605–7621 (2016).
5. K. Ebell, T. Nomokonova, M. Maturilli, and C. Ritter, "Radiative effect of clouds at Ny-Ålesund, svalbard, as inferred from ground-based remote sensing observations," J. Appl. Meteorol. Climatol. **59**(1), 3–22 (2020).
6. G. G. Mace, Q. Zhang, M. Vaughan, R. Marchand, G. Stephens, C. Trepte, and D. Winker, "A description of hydrometeor layer occurrence statistics derived from the first year of merged Cloudsat and CALIPSO data," J. Geophys. Res. Atmos. **114**, D00A26 (2009).

Optics EXPRESS

7. H. Nazaryan, M. P. McCormick, and W. P. Menzel, "Global characterization of cirrus clouds using CALIPSO data," J. Geophys. Res. Atmos. **113**(D16), D16211 (2008).
8. T. Nomokonova, K. Ebell, U. Löhnert, M. Maturilli, C. Ritter, and E. O'Connor, "Statistics on clouds and their relation to thermodynamic conditions at Ny-Ålesund using ground-based sensor synergy," Atmo. Chem. Phys. **19**(6), 4105–4126 (2019).
9. M. D. Shupe, V. P. Walden, E. Eloranta, T. Uttal, J. R. Campbell, S. M. Starkweather, and M. Shiobara, "Clouds at Arctic atmospheric observatories. Part I: Occurrence and macrophysical properties," J. Appl. Meteorol. Climatol. **50**(3), 626–644 (2011).
10. J. R. Campbell, S. Lolli, J. R. Lewis, Y. Gu, and E. J. Welton, "Daytime cirrus cloud top-of-the-atmosphere radiative forcing properties at a midlatitude site and their global consequences," J. Appl. Meteorol. Climatol. **55**(8), 1667–1679 (2016).
11. K. Sassen and J. M. Comstock, "A Midlatitude Cirrus Cloud Climatology from the Facility for Atmospheric Remote Sensing. Part III: Radiative Properties," J. Atmos. Sci. **58**(15), 2113–2127 (2001).
12. D. Josset, J. Pelon, A. Garnier, Y. Hu, M. Vaughan, P.-W. Zhai, R. Kuehn, and P. Lucker, "Cirrus optical depth and lidar ratio retrieval from combined CALIPSO-CloudSat observations using ocean surface echo," J. Geophys. Res. Atmos. **117**(D5), n/a (2012).
13. J. Gayet, I. Stachlewska, O. Jourdan, V. Shcherbakov, A. Schwarzenboeck, and R. Neuber, "Microphysical and optical properties of precipitating drizzle and ice particles obtained from alternated lidar and in situ measurements," Ann. Geophys. **25**(7), 1487–1497 (2007).
14. C. Platt, "Lidar and radiometric observations of cirrus clouds," J. Atmos. Sci. **30**(6), 1191–1204 (1973).
15. J. Delanoë and R. J. Hogan, "Combined CloudSat-CALIPSO-MODIS retrievals of the properties of ice clouds," J. Geophys. Res. Atmos. **115**(D14), D00H29 (2010).
16. S. Kox, L. Bugliaro, and A. Ostler, "Retrieval of cirrus cloud optical thickness and top altitude from geostationary remote sensing," Atmos. Meas. Tech. **7**(10), 3233–3246 (2014).
17. D. Wang, I. S. Stachlewska, J. Delanoë, D. Ene, X. Song, and D. Schüttemeyer, "Spatio-temporal discrimination of molecular, aerosol and cloud scattering and polarization using a combination of a Raman lidar, Doppler cloud radar and microwave radiometer," Opt. Express **28**(14), 20117–20134 (2020).
18. L. Mei, M. Vountas, L. Gómez-Chova, V. Rozanov, M. Jäger, W. Lotz, J. P. Burrows, and R. Hollmann, "A cloud masking algorithm for the xbaer aerosol retrieval using MERIS data," Remote Sens. Environ. **197**, 141–160 (2017).
19. S. Jafariserajehlou, L. Mei, M. Vountas, V. Rozanov, J. P. Burrows, and R. Hollmann, "A cloud identification algorithm over the Arctic for use with AATSR–SLSTR measurements," Atmos. Meas. Tech. **12**(2), 1059–1076 (2019).
20. M. D. King, S. Platnick, P. Yang, G. T. Arnold, M. A. Gray, J. C. Riedi, S. A. Ackerman, and K.-N. Liou, "Remote sensing of liquid water and ice cloud optical thickness and effective radius in the Arctic: Application of airborne multispectral mas data," J. Atmos. Ocean. Technol. **21**(6), 857–875 (2004).
21. L. Mei, V. Rozanov, M. Vountas, and J. P. Burrows, "The retrieval of ice cloud parameters from multi-spectral satellite observations of reflectance using a modified XBAER algorithm," Remote Sens. Environ. **215**, 128–144 (2018).
22. A. J. Heymsfield, M. Krämer, A. Luebke, P. Brown, D. J. Cziczo, C. Franklin, P. Lawson, U. Lohmann, G. McFarquhar, Z. Ulanowski, and K. V. Tricht, "Cirrus clouds," Meteorol. Monogr. **58**, 2.1–2.26 (2017).
23. S. Lolli, F. Madonna, M. Rosoldi, J. R. Campbell, E. J. Welton, J. R. Lewis, Y. Gu, and G. Pappalardo, "Impact of varying lidar measurement and data processing techniques in evaluating cirrus cloud and aerosol direct radiative effects," Atmos. Meas. Tech. **11**(3), 1639–1651 (2018).
24. M. D. Shupe, "A ground-based multisensor cloud phase classifier," Geophys. Res. Lett. **34**(22), L22809 (2007).
25. E. Jäkel, J. Walter, and M. Wendisch, "Thermodynamic phase retrieval of convective clouds: impact of sensor viewing geometry and vertical distribution of cloud properties," Atmos. Meas. Tech. **6**(3), 539–547 (2013).
26. M. Ceccaldi, J. Delanoë, R. Hogan, N. Pounder, A. Protat, and J. Pelon, "From CloudSat-CALIPSO to EarthCare: Evolution of the DARDAR cloud classification and its comparison to airborne radar-lidar observations," J. Geophys. Res. Atmos. **118**(14), 7962–7981 (2013).
27. J. R. Campbell, M. A. Vaughan, M. Oo, R. E. Holz, J. R. Lewis, and E. J. Welton, "Distinguishing cirrus cloud presence in autonomous lidar measurements," Atmos. Meas. Tech. **8**(1), 435–449 (2015).
28. H. Baars, P. Seifert, R. Engelmann, and U. Wandinger, "Target categorization of aerosol and clouds by continuous multiwavelength-polarization lidar measurements," Atmos. Meas. Tech. **10**(9), 3175–3201 (2017).
29. M. Di Pierro, L. Jaeglé, and T. L. Anderson, "Satellite observations of aerosol transport from East Asia to the Arctic: three case studies," Atmos. Chem. Phys. **11**(5), 2225–2243 (2011).
30. J. Huang, J. Guo, F. Wang, Z. Liu, M.-J. Jeong, H. Yu, and Z. Zhang, "CALIPSO inferred most probable heights of global dust and smoke layers," J. Geophys. Res. Atmos. **120**(10), 5085–5100 (2015).
31. Z. Liu, J. Kar, S. Zeng, J. Tackett, M. Vaughan, M. Avery, J. Pelon, B. Getzewich, K. P. Lee, B. Magill, A. Omar, P. Lucker, C. Trepte, and D. Winker, "Discriminating between clouds and aerosols in the CALIOP version 4.1 data products," Atmos. Meas. Tech. **12**(1), 703–734 (2019).
32. Z. Liu, M. Vaughan, D. Winker, C. Kittaka, B. Getzewich, R. Kuehn, A. Omar, K. Powell, C. Trepte, and C. Hostetler, "The CALIPSO lidar cloud and aerosol discrimination: Version 2 algorithm and initial assessment of performance," J. Atmos. Ocean. Technol. **26**(7), 1198–1213 (2009).

Optics EXPRESS

33. C. Di Biagio, J. Pelon, G. Ancellet, A. Bazureau, and V. Mariage, "Sources, load, vertical distribution, and fate of wintertime aerosols north of Svalbard from combined V4 CALIOP data, ground-based IAOOS lidar observations and trajectory analysis," J. Geophys. Res. Atmos. **123**(2), 1363–1383 (2018).
34. M. A. Avery, R. A. Ryan, B. J. Getzewich, M. A. Vaughan, D. M. Winker, Y. Hu, A. Garnier, J. Pelon, and C. A. Verhappen, "CALIOP V4 cloud thermodynamic phase assignment and the impact of near-nadir viewing angles," Atmos. Meas. Tech. **13**(8), 4539–4563 (2020).
35. D. M. Winker, M. A. Vaughan, A. Omar, Y. Hu, K. A. Powell, Z. Liu, W. H. Hunt, and S. A. Young, "Overview of the CALIPSO Mission and CALIOP Data Processing Algorithms," J. Atmos. Ocean. Technol. **26**(11), 2310–2323 (2009).
36. A. J. Illingworth, H. Barker, A. Beljaars, M. Ceccaldi, H. Chepfer, N. Clerbaux, J. Cole, J. Delanoë, C. Domenech, D. P. Donovan, S. Fukuda, M. Hirakata, R. J. Hogan, A. Huenerbein, P. Kollias, T. Kubota, T. Nakajima, T. Y. Nakajima, T. Nishizawa, Y. Ohno, H. Okamoto, R. Oki, S. K. M. Satoh, M. W. Shephard, A. Velázquez-Blázquez, U. Wandinger, T. Wehr, and G.-J. van Zadelhoff, "The EarthCARE satellite: The next step forward in global measurements of clouds, aerosols, precipitation, and radiation," Bull. Am. Meteorol. Soc. **96**(8), 1311–1332 (2015).
37. C. Platt, "Remote sounding of high clouds: I. Calculation of visible and infrared optical properties from lidar and radiometer measurements," J. Appl. Meteorol. **18**(9), 1130–1143 (1979).
38. S. A. Young, "Analysis of lidar backscatter profiles in optically thin clouds," Appl. Opt. **34**(30), 7019–7031 (1995).
39. E. Larroza, W. Nakaema, R. Bourayou, C. Hoareau, E. Landulfo, and P. Keckhut, "Towards an automatic lidar cirrus cloud retrieval for climate studies," Atmos. Meas. Tech. **6**(11), 3197–3210 (2013).
40. A. Ansmann, U. Wandinger, M. Riebesell, C. Weitkamp, and W. Michaelis, "Independent measurement of extinction and backscatter profiles in cirrus clouds by using a combined Raman elastic-backscatter lidar," Appl. Opt. **31**(33), 7113–7131 (1992).
41. S. Elouragini and P. H. Flamant, "Iterative method to determine an averaged backscatter-to-extinction ratio in cirrus clouds," Appl. Opt. **35**(9), 1512–1518 (1996).
42. K. Sassen and B. S. Cho, "Subvisual-thin cirrus lidar dataset for satellite verification and climatological research," J. Appl. Meteorol. **31**(11), 1275–1285 (1992).
43. A. Hoffmann, "Comparative aerosol studies based on multi-wavelength Raman lidar at Ny-Ålesund, Spitsbergen," https://epic.awi.de/id/eprint/29932/1/Hof2011g.pdf (2011).
44. C. Ritter, M. Angeles Burgos, C. Böckmann, D. Mateos, J. Lisok, K. Markowicz, B. Moroni, D. Cappelletti, R. Udisti, M. Maturilli, and R. Neuber, "Microphysical properties and radiative impact of an intense biomass burning aerosol event measured over Ny-Ålesund, Spitsbergen in July 2015," Tellus B **70**(1), 1–23 (2018).
45. K. J. Müller, C. Ritter, and K. Nakoudi, "Aerosol investigation during the Arctic haze season of 2018: Optical and hygroscopic properties," in *EPJ Web Conf.*, vol. 237 (2020), p. 02001.
46. K. Nakoudi, C. Ritter, C. Böckmann, D. Kunkel, O. Eppers, V. Rozanov, L. Mei, V. Pefanis, E. Jäkel, A. Herber, M. Maturilli, and R. Neuber, "Does the intra-Arctic modification of long-range transported aerosol affect the local radiative budget?(a case study)," Remote Sens. **12**(13), 2112 (2020).
47. I. Stachlewska and C. Ritter, "On retrieval of lidar extinction profiles using Two-stream and Raman techniques," Atmos. Chem. Phys. **10**(6), 2813–2824 (2010).
48. A. Lampert, C. Ritter, A. Hoffmann, J.-F. Gayet, G. Mioche, A. Ehrlich, A. Dörnbrack, M. Wendisch, and M. Shiobara, "Lidar characterization of the arctic atmosphere during ASTAR 2007: four cases studies of boundary layer, mixed-phase and multi-layer clouds," Atmos. Chem. Phys. **10**(6), 2847–2866 (2010).
49. M. Maturilli, "Radiosonde measurements from station Ny-Ålesund (2013-01)," https://doi.org/10.1594/PANGAEA.831286 (2014).
50. M. Maturilli, "Radiosonde measurements from station Ny-Ålesund (2015-04)," https://doi.org/10.1594/PANGAEA.863257 (2016).
51. M. Maturilli, "High resolution radiosonde measurements from station Ny-Ålesund (2019-01)," https://doi.org/10.1594/PANGAEA.899965 (2019).
52. M. D. Shupe, "Clouds at Arctic atmospheric observatories. Part II: Thermodynamic phase characteristics," J. Appl. Meteorol. Climatol. **50**(3), 645–661 (2011).
53. K. Nakoudi and C. Ritter, "AWI cirrus cloud retrieval scheme (v1.0.0)," https://zenodo.org/record/4265007#.X7JklnWYU5l (2020).
54. I. M. Brooks, "Finding boundary layer top: Application of a wavelet covariance transform to lidar backscatter profiles," J. Atmos. Ocean. Technol. **20**(8), 1092–1105 (2003).
55. D. Dionisi, P. Keckhut, G. L. Liberti, F. Cardillo, and F. Congeduti, "Midlatitude cirrus classification at Rome Tor Vergata through a multichannel Raman-Mie-Rayleigh lidar," Atmos. Chem. Phys. **13**(23), 11853–11868 (2013).
56. K. A. Voudouri, E. Giannakaki, M. Komppula, and D. Balis, "Variability in cirrus cloud properties using a polly^{XT} raman lidar over high and tropical latitudes," Atmos. Chem. Phys. **20**(7), 4427–4444 (2020).
57. K. Nakoudi, E. Giannakaki, A. Dandou, M. Tombrou, and M. Komppula, "Planetary boundary layer height by means of lidar and numerical simulations over New Delhi India," Atmos. Meas. Tech. **12**(5), 2595–2610 (2019).
58. D. Wang, I. S. Stachlewska, X. Song, B. Heese, and A. Nemuc, "Variability of the Boundary Layer Over an Urban Continental Site Based on 10 Years of Active Remote Sensing Observations in Warsaw," Remote Sens. **12**(2), 340 (2020).

Optics EXPRESS

59. P. Kokkalis, D. Alexiou, A. Papayannis, F. Rocadenbosch, O. Soupiona, P. I. Raptis, M. Mylonaki, C. G. Tzanis, and J. Christodoulakis, "Application and testing of the Extended-Kalman-Filtering technique for determining the Planetary Boundary-Layer Height over Athens, Greece," Bound.-Layer Meteorol. **176**(1), 125–147 (2020).
60. H. Baars, A. Ansmann, R. Engelmann, and D. Althausen, "Continuous monitoring of the boundary-layer top with lidar," Atmos. Chem. Phys. **8**(23), 7281–7296 (2008).
61. H. Baars, T. Kanitz, R. Engelmann, D. Althausen, B. Heese, M. Komppula, J. Preißler, M. Tesche, A. Ansmann, U. Wandinger, J.-H. Lim, J. Y. Ahn, I. S. Stachlewska, V. Amiridis, E. Marinou, P. Seifert, J. Hofer, A. Skupin, F. Schneider, S. Bohlmann, A. Foth, S. Bley, A. Pfüller, E. Giannakaki, H. Lihavainen, Y. Viisanen, R. K. Hooda, S. N. Pereira, D. Bortoli, F. Wagner, I. Mattis, L. Janicka, K. M. Markowicz, P. Achtert, P. Artaxo, T. Pauliquevis, R. A. F. Souza, V. P. Sharma, P. G. Van Zyl, J. P. Beukes, J. Sun, E. G. Rohwer, R. Deng, R.-E. Mamouri, and F. Zamorano, "An overview of the first decade of PollyNET: an emerging network of automated Raman-polarization lidars for continuous aerosol profiling," Atmos. Chem. Phys. **16**(8), 5111–5137 (2016).
62. J. R. Lanzante, "Resistant, robust and non-parametric techniques for the analysis of climate data: Theory and examples, including applications to historical radiosonde station data," Int. J. Climatol. **16**(11), 1197–1226 (1996).
63. J. D. Klett, "Stable analytical inversion solution for processing lidar returns," Appl. Opt. **20**(2), 211–220 (1981).
64. F. G. Fernald, "Analysis of atmospheric lidar observations: some comments," Appl. Opt. **23**(5), 652–653 (1984).
65. V. S. Ryaben'kii and S. V. Tsynkov, *A theoretical introduction to numerical analysis* (CRC Press, 2006).
66. E. Giannakaki, D. Balis, V. Amiridis, and S. Kazadzis, "Optical and geometrical characteristics of cirrus clouds over a Southern European lidar station," Atmos. Chem. Phys. **7**(21), 5519–5530 (2007).
67. S. K. Das, C. W. Chiang, and J. B. Nee, "Characteristics of cirrus clouds and its radiative properties based on lidar observation over Chung-Li, Taiwan," Atmos. Res. **93**(4), 723–735 (2009).
68. D. A. Gouveia, B. Barja, H. M. Barbosa, P. Seifert, H. Baars, T. Pauliquevis, and P. Artaxo, "Optical and geometrical properties of cirrus clouds in Amazonia derived from 1 year of ground-based lidar measurements," Atmos. Chem. Phys. **17**(5), 3619–3636 (2017).
69. C. Ritter, R. Neuber, A. Schulz, K. Markowicz, I. Stachlewska, J. Lisok, P. Makuch, P. Pakszys, P. Markuszewski, A. Rozwadowska, T. Petelski, T. Zielinski, S. Becagli, R. Traversi, R. Udisti, and M. Gausa, "2014 iAREA campaign on aerosol in Spitsbergen–part 2: Optical properties from raman-lidar and in-situ observations at Ny-Ålesund," Atmos. Environ. **141**, 1–19 (2016).
70. W. Chen, C. W. Chiang, and J. B. Nee, "Lidar ratio and depolarization ratio for cirrus clouds," Appl. Opt. **41**(30), 6470–6476 (2002).
71. A. Borovoi, A. Konoshonkin, and N. Kustova, "Backscatter ratios for arbitrary oriented hexagonal ice crystals of cirrus clouds," Opt. Lett. **39**(19), 5788–5791 (2014).
72. H. Okamoto, K. Sato, A. Borovoi, H. Ishimoto, K. Masuda, A. Konoshonkin, and N. Kustova, "Interpretation of lidar ratio and depolarization ratio of ice clouds using spaceborne high-spectral-resolution polarization lidar," Opt. Express **27**(25), 36587–36600 (2019).
73. H. Okamoto, K. Sato, A. Borovoi, H. Ishimoto, K. Masuda, A. Konoshonkin, and N. Kustova, "Wavelength dependence of ice cloud backscatter properties for space-borne polarization lidar applications," Opt. Express **28**(20), 29178–29191 (2020).
74. A. Savitzky and M. J. Golay, "Smoothing and differentiation of data by simplified least squares procedures," Anal. Chem. **36**(8), 1627–1639 (1964).
75. E. W. Eloranta, "Practical model for the calculation of multiply scattered lidar returns," Appl. Opt. **37**(12), 2464–2472 (1998).
76. Z. Wang and K. Sassen, "Cirrus Cloud Microphysical Property Retrieval Using Lidar and Radar Measurements. Part II: Midlatitude Cirrus Microphysical and Radiative Properties," J. Atmos. Sci. **59**(14), 2291–2302 (2002).
77. U. Wandinger, "Multiple-scattering influence on extinction- and backscatter-coefficient measurements with Raman and high-spectral-resolution lidars," Appl. Opt. **37**(3), 417–427 (1998).
78. M. Iarlori, F. Madonna, V. Rizi, T. Trickl, and A. Amodeo, "Effective resolution concepts for lidar observations," Atmos. Meas. Tech. **8**(12), 5157–5176 (2015).
79. I. S. Stachlewska, M. Costa-Surós, and D. Althausen, "Raman lidar water vapor profiling over Warsaw, Poland," Atmos. Res. **194**, 258–267 (2017).
80. E. J. Welton, J. R. Campbell, J. D. Spinhirne, and V. S. Scott III, "Global monitoring of clouds and aerosols using a network of micropulse lidar systems," in *Lidar Remote Sensing for Industry and Environment Monitoring*, vol. 4153 (International Society for Optics and Photonics, 2001), pp. 151–158.
81. F. Mao, W. Gong, and Z. Zhu, "Simple multiscale algorithm for layer detection with lidar," Appl. Opt. **50**(36), 6591–6598 (2011).